2012

Three-dimensional anisotropic seismic wave modelling in spherical coordinates by a collocated-grid finite-difference method

Wei Zhang
University of Rhode Island

Yang Shen
University of Rhode Island, yshen@uri.edu

Li Zhao
University of Rhode Island

Citation/Publisher Attribution

Wei Zhang, Yang Shen, Li Zhao; Three-dimensional anisotropic seismic wave modelling in spherical coordinates by a collocated-grid finite-difference method, *Geophysical Journal International*, Volume 188, Issue 3, 1 March 2012, Pages 1359–1381, https://doi.org/10.1111/j.1365-246X.2011.05331.x
Available at: https://doi.org/10.1111/j.1365-246X.2011.05331.x

Three-dimensional anisotropic seismic wave modelling in spherical coordinates by a collocated-grid finite-difference method

Geophysical Journal International

Geophys. J. Int. (2012) **188,** 1359–1381 doi: 10.1111/j.1365-246X.2011.05331.x

Three-dimensional anisotropic seismic wave modelling in spherical coordinates by a collocated-grid finite-difference method

Wei Zhang,[1] Yang Shen[1] and Li Zhao[1,2]

[1] *Graduate School of Oceanography, University of Rhode Island, RI* 02882, *USA. E-mail: yshen@gso.uri.edu*
[2] *Institute of Earth Sciences, Academia Sinica, Taipei* 11529, *Taiwan*

Accepted 2011 December 8. Received 2011 December 7; in original form 2011 August 15

SUMMARY

To simulate seismic wave propagation in the spherical Earth, the Earth's curvature has to be taken into account. This can be done by solving the seismic wave equation in spherical coordinates by numerical methods. In this paper, we use an optimized, collocated-grid finite-difference scheme to solve the anisotropic velocity–stress equation in spherical coordinates. To increase the efficiency of the finite-difference algorithm, we use a non-uniform grid to discretize the computational domain. The grid varies continuously with smaller spacing in low velocity layers and thin layer regions and with larger spacing otherwise. We use stress-image setting to implement the free surface boundary condition on the stress components. To implement the free surface boundary condition on the velocity components, we use a compact scheme near the surface. If strong velocity gradient exists near the surface, a lower-order scheme is used to calculate velocity difference to stabilize the calculation. The computational domain is surrounded by complex-frequency shifted perfectly matched layers implemented through auxiliary differential equations (ADE CFS-PML) in a local Cartesian coordinate. We compare the simulation results with the results from the normal mode method in the isotropic and anisotropic models and verify the accuracy of the finite-difference method.

Key words: Numerical solutions; Seismic anisotropy; Computational seismology; Wave propagation.

1 INTRODUCTION

Numerical modelling of seismic wave propagation is important to the study of the Earth structure (Igel 1999; Fichtner *et al.* 2009a,b). For seismic wave modelling at global or regional scales, the effect of Earth's curvature on wave propagation should be taken into account. This can be achieved by either solving the wave equation in a global Cartesian coordinate with the Earth surface as an irregular surface (e.g. Komatitsch & Tromp 2002a,b), or directly solving the wave equation in spherical coordinates in 3-D (e.g. Igel 1999; Fichtner *et al.* 2009a,b) or cylindrical coordinate in 2-D (e.g. Wang *et al.* 2001). Several numerical methods, including the finite-difference method (FDM; e.g. Igel & Weber 1995, 1996; Igel *et al.* 2002; Jahnke *et al.* 2008), pseudospectral method (PSM; e.g. Igel 1999; Wang *et al.* 2001) and spectral-element method (SEM; e.g. Komatitsch & Tromp 2002a,b; Nissen-Meyer *et al.* 2006; Fichtner *et al.* 2009a,b), have been used to model wave propagation in the global Earth or spherical sections.

FDM has been one of the most popular numerical methods used in seismological studies for several reasons. The operator of FDM only involves several adjacent gridpoints. This local character in parametrize is well suited for highly heterogeneous media and can be easily parallelized on distributed memory high-performance computers. It does not require meshes to align with interior interface topography (Moczo *et al.* 2002) and, thus, minimizes the effort in grid generation.

Particularly, the staggered-grid finite-difference scheme is widely used in the context of seismic wave modelling (e.g. Madariaga 1976; Virieux 1984, 1986; Levander 1988; Graves 1996; Kristek *et al.* 2002), in which different components of the velocity vector and stress matrix are defined at different positions in a rectangular cell. Several studies have used this staggered-grid finite-difference scheme for seismic wave modelling in spherical coordinate systems (e.g. Igel & Weber 1995, 1996; Nissen-Meyer 2001; Igel *et al.* 2002; Jahnke *et al.* 2008). However, the staggered-grid FDM is only ideal for solving elastodynamic equations with Cartesian grids. In spherical coordinates, there is no practical way to distribute the wavefield components in a staggered fashion that every component is just required at its definition locations. Interpolations have to be used which reduce the overall accuracy of the scheme (Igel & Weber 1995). In this study, we propose to use an optimized collocated-grid finite-difference scheme (Hixon 1997; Zhang & Chen 2006, 2011; Zhu *et al.* 2009) to solve the first-order hyperbolic anisotropic seismic wave equation with a velocity–stress formulation in spherical coordinates, thus, no interpolation is required.

To improve computational efficiency, we employ a non-uniform grid to avoid unnecessarily small grids at great depth. Our scheme also includes a higher-order surface implementation and an efficient perfectly matched layers (PML) implementation.

To begin with, we introduce the anisotropic elastic wave equation in spherical coordinates. Then, we describe how to use the collocated-grid finite-difference scheme to solve the wave equation, the extension of the scheme to non-uniform grids and the free surface boundary condition implementation. Finally, the proposed scheme is verified through comparisons against solutions from the normal mode method in both the isotropic and anisotropic Preliminary Reference Earth Model (PREM; Dziewonski & Anderson 1981).

2 ANISOTROPIC ELASTIC WAVE EQUATIONS IN SPHERICAL COORDINATES

It is straightforward to take the effect of the Earth's curvature into account by solving seismic wave equations in a spherical coordinate (θ, ϕ, r; Fig. 1), where

(1) θ is the colatitude, the zenith angle measured from the North Pole and positive towards south;
(2) ϕ is the longitude angle and
(3) r is the radial distance measured from the centre of the Earth and positive outward.

The position of a point in this spherical coordinate is expressed as $\mathbf{r} = \mathbf{r}(\theta, \phi, r) = \theta\hat{\mathbf{e}}_\theta + \phi\hat{\mathbf{e}}_\phi + r\hat{\mathbf{e}}_r$, where $\hat{\mathbf{e}}_\theta$, $\hat{\mathbf{e}}_\phi$ and $\hat{\mathbf{e}}_r$ are the unit vectors of the spherical coordinate axes at the point.

The elastic seismic wave generated by an external force or internal earthquake in a linearly anisotropic elastic medium is governed by the momentum equation,

$$\rho\mathbf{u}_{,tt} = \nabla\cdot\boldsymbol{\sigma} + \mathbf{f}, \tag{1}$$

stress–strain relation (constitutive relation, Hooke's law)

$$\boldsymbol{\sigma} = \mathbf{c} : \boldsymbol{\varepsilon}, \tag{2}$$

infinitesimal strain tensor,

$$\boldsymbol{\varepsilon} = \frac{1}{2}\left[\nabla\mathbf{u} + (\nabla\mathbf{u})^T\right], \tag{3}$$

and the initial and boundary conditions,

$$\mathbf{u}(\mathbf{r}, 0) = 0, \qquad \mathbf{v}(\mathbf{r}, 0) = 0, \qquad \boldsymbol{\sigma}(R, t)\cdot\hat{\mathbf{n}}|_{r=R} = 0. \tag{4}$$

In the above equations, t is time. A comma followed by t or tt in subscripts means the first-order or second-order derivative with respect to time. The displacement vectors are denoted by $\mathbf{u} = u_i(\mathbf{r}, t)\hat{\mathbf{e}}_i$ (in this section, index $i, j, k, l \in \{\theta, \phi, r\}$ and the Einstein summation convention for repeated indices is adopted). The velocity vectors is $\mathbf{v} = \mathbf{u}_{,t}$, $\boldsymbol{\sigma} = \sigma_{ij}(\mathbf{r}, t)\hat{\mathbf{e}}_i\hat{\mathbf{e}}_j$ the stress tensor, $\boldsymbol{\varepsilon} = \varepsilon_{ij}(\mathbf{r}, t)\hat{\mathbf{e}}_i\hat{\mathbf{e}}_j$ the strain tensor, $\mathbf{f} = f_i(\mathbf{r}, t)\hat{\mathbf{e}}_i$ the source term, $\hat{\mathbf{n}}|_{r=R}$ the unit vector of normal direction of the surface, $\rho = \rho(\mathbf{r})$ the mass density, $\mathbf{c} = c_{ijkl}(\mathbf{r})\hat{\mathbf{e}}_i\hat{\mathbf{e}}_j\hat{\mathbf{e}}_k\hat{\mathbf{e}}_l$ the fourth-order stiffness tensor, which has 21 independent parameters for the most general anisotropic medium. R denotes the radius of the surface. Using the Voigt notation to map the index pairs into a single index through,

$$\{\theta\theta\}\to 1,\ \{\phi\phi\}\to 2,\ \{rr\}\to 3,\ \{\phi r\}\to 4,\ \{\theta r\}\to 5,\ \{\theta\phi\}\to 6, \tag{5}$$

we can rewrite the fourth-order stiffness tensor $\mathbf{c}$ as a symmetric second-order tensor $\mathbf{C}$,

$$C_{mn} = c_{ijkl}, \tag{6}$$

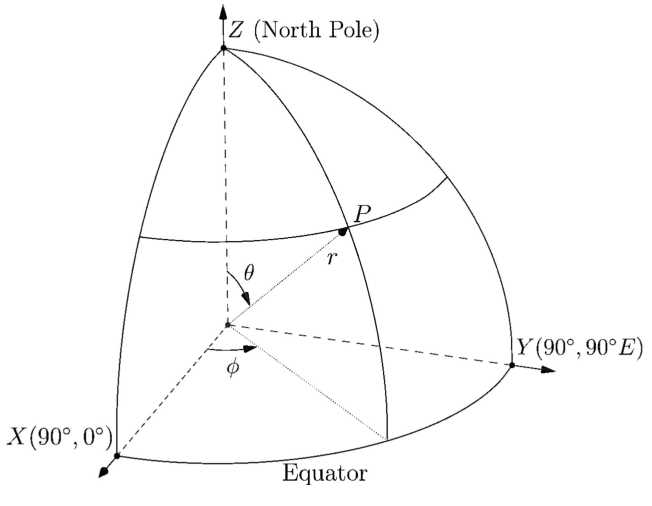

Figure 1. Spherical coordinate (θ, ϕ, r).

where $\{ij\} \rightarrow m$, $\{kl\} \rightarrow n$; $m, n \in \{1, 2, 3, 4, 5, 6\}$. Expressions of **C** for general anisotropic, isotropic and vertical transversely isotropic (VTI) media are in Appendix A.

Adopting the Voigt notation, we rewrite eq. (1-3) into a velocity–stress first-order hyperbolic formulation in spherical coordinates (Nissen-Meyer 2001; Igel *et al.* 2002; Fichtner 2011), using the general anisotropic medium as an example,

$$\rho v_{\theta,t} = \frac{1}{r}\sigma_{\theta\theta,\theta} + \frac{1}{r\sin\theta}\sigma_{\theta\phi,\phi} + \sigma_{\theta r,r} + \frac{1}{r}(3\sigma_{\theta r} + \sigma_{\theta\theta}\cot\theta - \sigma_{\phi\phi}\cot\theta) + f_\theta, \tag{7}$$

$$\rho v_{\phi,t} = \frac{1}{r}\sigma_{\theta\phi,\theta} + \frac{1}{r\sin\theta}\sigma_{\phi\phi,\phi} + \sigma_{\phi r,r} + \frac{1}{r}(2\sigma_{\theta\phi}\cot\theta + 3\sigma_{\phi r}) + f_\phi, \tag{8}$$

$$\rho v_{r,t} = \frac{1}{r}\sigma_{\theta r,\theta} + \frac{1}{r\sin\theta}\sigma_{\phi r,\phi} + \sigma_{rr,r} + \frac{1}{r}(2\sigma_{rr} - \sigma_{\theta\theta} - \sigma_{\phi\phi} + \sigma_{\theta r}\cot\theta) + f_r, \tag{9}$$

$$\sigma_{\theta\theta,t} = C_{11}\varepsilon_{\theta\theta,t} + C_{12}\varepsilon_{\phi\phi,t} + C_{13}\varepsilon_{rr,t} + 2C_{14}\varepsilon_{\phi r,t} + 2C_{15}\varepsilon_{\theta r,t} + 2C_{16}\varepsilon_{\theta\phi,t} - M_{\theta\theta,t}, \tag{10}$$

$$\sigma_{\phi\phi,t} = C_{12}\varepsilon_{\theta\theta,t} + C_{22}\varepsilon_{\phi\phi,t} + C_{23}\varepsilon_{rr,t} + 2C_{24}\varepsilon_{\phi r,t} + 2C_{25}\varepsilon_{\theta r,t} + 2C_{26}\varepsilon_{\theta\phi,t} - M_{\phi\phi,t}, \tag{11}$$

$$\sigma_{rr,t} = C_{13}\varepsilon_{\theta\theta,t} + C_{23}\varepsilon_{\phi\phi,t} + C_{33}\varepsilon_{rr,t} + 2C_{34}\varepsilon_{\phi r,t} + 2C_{35}\varepsilon_{\theta r,t} + 2C_{36}\varepsilon_{\theta\phi,t} - M_{rr,t}, \tag{12}$$

$$\sigma_{\phi r,t} = C_{14}\varepsilon_{\theta\theta,t} + C_{24}\varepsilon_{\phi\phi,t} + C_{34}\varepsilon_{rr,t} + 2C_{44}\varepsilon_{\phi r,t} + 2C_{45}\varepsilon_{\theta r,t} + 2C_{46}\varepsilon_{\theta\phi,t} - M_{\phi r,t}, \tag{13}$$

$$\sigma_{\theta r,t} = C_{15}\varepsilon_{\theta\theta,t} + C_{25}\varepsilon_{\phi\phi,t} + C_{35}\varepsilon_{rr,t} + 2C_{45}\varepsilon_{\phi r,t} + 2C_{55}\varepsilon_{\theta r,t} + 2C_{56}\varepsilon_{\theta\phi,t} - M_{\theta r,t}, \tag{14}$$

$$\sigma_{\theta\phi,t} = C_{16}\varepsilon_{\theta\theta,t} + C_{26}\varepsilon_{\phi\phi,t} + C_{36}\varepsilon_{rr,t} + 2C_{46}\varepsilon_{\phi r,t} + 2C_{56}\varepsilon_{\theta r,t} + 2C_{66}\varepsilon_{\theta\phi,t} - M_{\theta\phi,t}, \tag{15}$$

$$\varepsilon_{\theta\theta,t} = \frac{1}{r}v_{\theta,\theta} + \frac{1}{r}v_r, \tag{16}$$

$$\varepsilon_{\phi\phi,t} = \frac{1}{r\sin\theta}v_{\phi,\phi} + \frac{\cot\theta}{r}v_\theta + \frac{1}{r}v_r, \tag{17}$$

$$\varepsilon_{rr,t} = v_{r,r}, \tag{18}$$

$$\varepsilon_{\phi r,t} = \frac{1}{2}\left(\frac{1}{r\sin\theta}v_{r,\phi} + v_{\phi,r} - \frac{1}{r}v_\phi\right), \tag{19}$$

$$\varepsilon_{\theta r,t} = \frac{1}{2}\left(\frac{1}{r}v_{r,\theta} + v_{\theta,r} - \frac{1}{r}v_\theta\right), \tag{20}$$

$$\varepsilon_{\theta\phi,t} = \frac{1}{2}\left(\frac{1}{r}v_{\phi,\theta} + \frac{1}{r\sin\theta}v_{\theta,\phi} - \frac{\cot\theta}{r}v_\phi\right), \tag{21}$$

where $M_{\theta\theta}$, $M_{\phi\phi}$, M_{rr}, $M_{\theta r}$, $M_{\phi r}$ and $M_{\theta\phi}$ are the components of the source moment tensor. A comma followed by θ, ϕ, r in subscript means a partial derivative with respect to θ, ϕ or r.

For the convenience of the description of the finite-difference scheme in the next section, we rewrite the velocity–stress equations (eqs 7–21) in a compact vector–matrix form,

$$\mathbf{U}_{,t} = \mathbf{A}_\theta\mathbf{U}_{,\theta} + \mathbf{A}_\phi\mathbf{U}_{,\phi} + \mathbf{A}_r\mathbf{U}_{,r} + \mathbf{A}\mathbf{U} + \mathbf{F}, \tag{22}$$

where **U** is the velocity–stress vector,

$$\mathbf{U} = (v_\theta, v_\phi, v_r, \sigma_{\theta\theta}, \sigma_{\phi\phi}, \sigma_{rr}, \sigma_{\phi r}, \sigma_{\theta r}, \sigma_{\theta\phi})^T,$$

F is the source term vector,

$$\mathbf{F} = (f_\theta, f_\phi, f_r, -M_{\theta\theta,t}, -M_{\phi\phi,t}, -M_{rr,t}, -M_{\theta r,t}, -M_{\phi r,t}, -M_{\theta\phi,t})^T,$$

and the coefficient matrices $\mathbf{A}_\theta$, $\mathbf{A}_\phi$, $\mathbf{A}_r$ and **A** can be found in Appendix B.

3 COLLOCATED-GRID DISPERSION RELATION PRESERVING (DRP)/OPT MACCORMACK FINITE-DIFFERENCE SCHEME

The staggered-grid FDM has been successfully used to solve the first-order hyperbolic elastic wave equations in the Cartesian coordinate (e.g. Madariaga 1976; Virieux 1984, 1986; Levander 1988; Graves 1996; Kristek *et al.* 2002). However, when used for general anisotropic media or on non-Cartesian grids, the staggered-grid finite-difference (FDTD) method requires interpolation to calculate the quantities needed at places different from its definition locations, which limits the overall accuracy (Magnier *et al.* 1994; Igel *et al.* 1995). In contrast, collocated-grid finite-difference schemes, in which all the components of the velocity–stress vector are located at the same grid position, can be used in general anisotropic media and general curvilinear grids. One popular and well-tested collocated-grid scheme is the MacCormack-type scheme (MacCormack 1969; Hixon 1997). The MacCormack-type scheme has inherent dissipation that has a negligible effect on the physical solution but damps the spurious short-wavelength numerical (non-physical) waves generated by media discontinuities, computational domain boundaries, grid discontinuities and other computational irregularities. More importantly, the inherent dissipation can also eliminate the odd-even decoupling phenomenon (grid-to-grid oscillation; Patankar 1980, pp. 115–117) that exists in the collocated-grid central finite-difference schemes.

In the context of seismic wave modelling, a higher-order extension of the MacCormack scheme (Gottlieb & Turkel 1976), which has second-order accuracy in time and fourth-order accuracy in space, is commonly used (Bayliss *et al.* 1986; Xie & Yao 1988; Tsingas *et al.* 1990; Vafidis *et al.* 1992; Dai *et al.* 1995). A more accurate and optimized MacCormack-type scheme was developed in Hixon (1997). He used the DRP methodology of Tam & Webb (1993) to optimize the dispersion error of the added central difference, and utilized the same methodology to optimize the dissipation error of the one-sided differences to develop the so-called DRP/opt MacCormack scheme, which has been used to model 2-D and 3-D seismic wave in the presence of surface topography (Zhang & Chen 2006, 2011; Zhang *et al.* 2008) and in anisotropic media (Zhu *et al.* 2009).

In MacCormack-type schemes, the central difference operator is split into forward and backward one-sided differences. The one-sided differences are alternately used in a multistage Runge–Kutta-type time integration method, and the central difference is recovered when the forward and backward differences are added together at the last time stage. The fourth-order Runge–Kutta scheme for the time integration of the first-order hyperbolic systems (eq. 22) can be written as,

$$\begin{aligned}
\mathbf{U}^{(1)} &= \mathbf{U}^{n}\\
\mathbf{U}^{(2)} &= \mathbf{U}^{n} + \alpha_2 \Delta t \hat{L}(\mathbf{U}^{(1)})\\
\mathbf{U}^{(3)} &= \mathbf{U}^{n} + \alpha_3 \Delta t \hat{L}(\mathbf{U}^{(2)})\\
\mathbf{U}^{(4)} &= \mathbf{U}^{n} + \alpha_4 \Delta t \hat{L}(\mathbf{U}^{(3)})\\
\mathbf{U}^{n+1} &= \mathbf{U}^{n} + \Delta t[\beta_1 \hat{L}(\mathbf{U}^{(1)}) + \beta_2 \hat{L}(\mathbf{U}^{(2)}) + \beta_3 \hat{L}(\mathbf{U}^{(3)}) + \beta_4 \hat{L}(\mathbf{U}^{(4)})],
\end{aligned} \tag{23}$$

where the coefficients $\alpha_2 = 0.5, \alpha_3 = 0.5, \alpha_4 = 1, \beta_1 = \frac{1}{6}, \beta_2 = \frac{1}{3}, \beta_3 = \frac{1}{3}$ and $\beta_4 = \frac{1}{6}$, and

$$\hat{L}(\mathbf{U}) = \mathbf{A}_\theta L_\theta(\mathbf{U}) + \mathbf{A}_\phi L_\phi(\mathbf{U}) + \mathbf{A}_r L_r(\mathbf{U}) + \mathbf{AU} + \mathbf{F} \tag{24}$$

represent the 3-D discretized spatial difference operators, L_θ, L_ϕ and L_r are the difference operators for derivatives along θ-axis, ϕ-axis and r-axis. The DRP/opt MacCormack scheme alternately uses following forward and backward difference operators (using derivatives with respect to θ-axis as an example) in different stages of the Runge–Kutta scheme,

$$L_\theta^F(\mathbf{U})_i = \frac{1}{\Delta\theta} \sum_{n=-1}^{3} a_n \mathbf{U}_{i+n}, \tag{25}$$

$$L_\theta^B(\mathbf{U})_i = \frac{1}{\Delta\theta} \sum_{n=-1}^{3} -a_n \mathbf{U}_{i-n}, \tag{26}$$

where the superscript F and B on L_θ denotes biased forward and backward difference operators, respectively. The coefficients $a_{-1} = -0.30874$, $a_0 = -0.6326$, $a_1 = 1.2330$, $a_2 = -0.3334$ and $a_3 = 0.04168$ are obtained by minimizing the dissipation error at eight points or more per wavelength (Hixon 1997), and have formal fourth-order dispersion accuracy. If we denote the 3-D biased difference operators as

$$\hat{L}^{FFF} = \mathbf{A}_\theta L_\theta^F(\mathbf{U}) + \mathbf{A}_\phi L_\phi^F(\mathbf{U}) + \mathbf{A}_r L_r^F(\mathbf{U}) + \mathbf{AU} + \mathbf{F}, \tag{27}$$

$$\hat{L}^{BBB} = \mathbf{A}_\theta L_\theta^B(\mathbf{U}) + \mathbf{A}_\phi L_\phi^B(\mathbf{U}) + \mathbf{A}_r L_r^B(\mathbf{U}) + \mathbf{AU} + \mathbf{F}, \tag{28}$$

the DRP/opt MacCormack scheme used with the fourth-order Runge–Kutta stepping scheme can be written as,

$$\begin{aligned}
\mathbf{U}^{(1)} &= \mathbf{U}^{n}\\
\mathbf{U}^{(2)} &= \mathbf{U}^{n} + \alpha_2 \Delta t \hat{L}^{FFF}(\mathbf{U}^{(1)})\\
\mathbf{U}^{(3)} &= \mathbf{U}^{n} + \alpha_3 \Delta t \hat{L}^{BBB}(\mathbf{U}^{(2)})\\
\mathbf{U}^{(4)} &= \mathbf{U}^{n} + \alpha_4 \Delta t \hat{L}^{FFF}(\mathbf{U}^{(3)})\\
\mathbf{U}^{n+1} &= \mathbf{U}^{n} + \Delta t[\beta_1 \hat{L}^{FFF}(\mathbf{U}^{(1)}) + \beta_2 \hat{L}^{BBB}(\mathbf{U}^{(2)}) + \beta_3 \hat{L}^{FFF}(\mathbf{U}^{(3)}) + \beta_4 \hat{L}^{BBB}(\mathbf{U}^{(4)})].
\end{aligned} \tag{29}$$

In this paper, we use the following expression to represent the above fourth-order Runge–Kutta step (eq. 29),

$$\mathbf{U}^{n+1} = \hat{L}^{FFF} \hat{L}^{BBB} \hat{L}^{FFF} \hat{L}^{BBB} \mathbf{U}^{n}. \tag{30}$$

It should be noted that the start order of the biased difference operators is interchanged every step to avoid numerical biasing, resulting in a two-step sequence,

$$\begin{aligned}
\mathbf{U}^{n+1} &= \hat{L}^{FFF} \hat{L}^{BBB} \hat{L}^{FFF} \hat{L}^{BBB} \mathbf{U}^{n}\\
\mathbf{U}^{n+2} &= \hat{L}^{BBB} \hat{L}^{FFF} \hat{L}^{BBB} \hat{L}^{FFF} \mathbf{U}^{n+1}.
\end{aligned} \tag{31}$$

There are other three possible pairs of the 3-D MacCormack-type difference operators,

$$\begin{aligned}\mathbf{U}^{n+1} &= \hat{L}^{FFB}\hat{L}^{BBF}\hat{L}^{FFB}\hat{L}^{BBF}\mathbf{U}^{n}\\ \mathbf{U}^{n+2} &= \hat{L}^{BBF}\hat{L}^{FFB}\hat{L}^{BBF}\hat{L}^{FFB}\mathbf{U}^{n+1},\end{aligned} \tag{32}$$

$$\begin{aligned}\mathbf{U}^{n+1} &= \hat{L}^{FBF}\hat{L}^{BFB}\hat{L}^{FBF}\hat{L}^{BFB}\mathbf{U}^{n}\\ \mathbf{U}^{n+2} &= \hat{L}^{BFB}\hat{L}^{FBF}\hat{L}^{BFB}\hat{L}^{FBF}\mathbf{U}^{n+1},\end{aligned} \tag{33}$$

$$\begin{aligned}\mathbf{U}^{n+1} &= \hat{L}^{BFF}\hat{L}^{FBB}\hat{L}^{BFF}\hat{L}^{FBB}\mathbf{U}^{n}\\ \mathbf{U}^{n+2} &= \hat{L}^{FBB}\hat{L}^{BFF}\hat{L}^{FBB}\hat{L}^{BFF}\mathbf{U}^{n+1}.\end{aligned} \tag{34}$$

We could use two, three or all four pairs of the 3-D MacCormack-type operators, or many other possible combinations of them. We found that the following combination of all four pairs of the operators in an eight time step sequence has better resolution around the source region,

$$\begin{aligned}\mathbf{U}^{n+1} &= \hat{L}^{BBB}\hat{L}^{FFF}\hat{L}^{BBB}\hat{L}^{FFF}\mathbf{U}^{n}\\ \mathbf{U}^{n+2} &= \hat{L}^{FFB}\hat{L}^{BBF}\hat{L}^{FFB}\hat{L}^{BBF}\mathbf{U}^{n+1}\\ \mathbf{U}^{n+3} &= \hat{L}^{FFF}\hat{L}^{BBB}\hat{L}^{FFF}\hat{L}^{BBB}\mathbf{U}^{n+2}\\ \mathbf{U}^{n+4} &= \hat{L}^{BBF}\hat{L}^{FFB}\hat{L}^{BBF}\hat{L}^{FFB}\mathbf{U}^{n+3}\\ \mathbf{U}^{n+5} &= \hat{L}^{BFB}\hat{L}^{FBF}\hat{L}^{BFB}\hat{L}^{FBF}\mathbf{U}^{n+4}\\ \mathbf{U}^{n+6} &= \hat{L}^{FBB}\hat{L}^{BFF}\hat{L}^{FBB}\hat{L}^{BFF}\mathbf{U}^{n+5}\\ \mathbf{U}^{n+7} &= \hat{L}^{FBF}\hat{L}^{BFB}\hat{L}^{FBF}\hat{L}^{BFB}\mathbf{U}^{n+6}\\ \mathbf{U}^{n+8} &= \hat{L}^{BFF}\hat{L}^{FBB}\hat{L}^{BFF}\hat{L}^{FBB}\mathbf{U}^{n+7}.\end{aligned} \tag{35}$$

The stability criterion of the DRP/opt MacCormack with the fourth-order Runge–Kutta scheme is,

$$\Delta t < 1.32\frac{\Delta h}{v_{\max}} \tag{36}$$

in 1-D (Hixon & Turkel 2000) and

$$\Delta t < 0.76\frac{\Delta h}{v_{\max}} \tag{37}$$

in 3-D, where Δh is the grid size and $v_{\max}$ is the maximum wave speed.

4 NON-UNIFORM GRID

When the seismic wave speed in the medium varies over a wide range, the efficiency of the finite-difference scheme is drastically reduced if the grid size is constant in all three spatial directions. This happens when the *S* wave speed is very low near the surface, such as in a sedimentary basin, where a small grid size is needed. To increase the efficiency of the finite-difference algorithm, we use a grid with non-uniform grid spacing to discretize the computational domain, as shown in Fig. 2. The grid varies continuously with smaller spacing in the low velocity region and thin layers and larger spacing otherwise. The non-uniform grid can improve computational efficiency in two ways, (1) a smaller number of radial gridpoints reduces memory requirement and reduces computational time since the amount of computation is proportional to the number of gridpoints; (2) the non-uniform grid allows for a longer distance to its diagonal plane than a uniform grid in the deeper high velocity regions, yielding a larger time step than the uniform grid configuration. The distance to the diagonal plane of the grid is the effective 1-D grid size that determines the time step.

To numerically update the velocity–stress equations on this non-uniform grid, one can modify the finite-difference operator coefficients according to variable grid spacing (Pitarka 1999) or transform the non-uniform grid to a uniform reference grid via the coordinate mapping,

$$\theta = \theta(\xi) \qquad \phi = \phi(\eta) \qquad r = r(\zeta), \tag{38}$$

where (ξ, η, ζ) is the location of points in the reference coordinate. The velocity–stress equations (eqs 7–21) can be transformed into the reference coordinate using the chain rule,

$$\rho v_{\theta,t} = \frac{1}{r}\xi_{,\theta}\sigma_{\theta\theta,\xi} + \frac{1}{r\sin\theta}\eta_{,\phi}\sigma_{\theta\phi,\eta} + \zeta_{,r}\sigma_{\theta r,\zeta} + \frac{1}{r}(3\sigma_{\theta r} + \sigma_{\theta\theta}\cot\theta - \sigma_{\phi\phi}\cot\theta) + f_\theta, \tag{39}$$

$$\rho v_{\phi,t} = \frac{1}{r}\xi_{,\theta}\sigma_{\theta\phi,\xi} + \frac{1}{r\sin\theta}\eta_{,\phi}\sigma_{\phi\phi,\eta} + \zeta_{,r}\sigma_{\phi r,\zeta} + \frac{1}{r}(2\sigma_{\theta\phi}\cot\theta + 3\sigma_{\phi r}) + f_\phi, \tag{40}$$

$$\rho v_{r,t} = \frac{1}{r}\xi_{,\theta}\sigma_{\theta r,\xi} + \frac{1}{r\sin\theta}\eta_{,\phi}\sigma_{\phi r,\eta} + \zeta_{,r}\sigma_{rr,\zeta} + \frac{1}{r}(2\sigma_{rr} - \sigma_{\theta\theta} - \sigma_{\phi\phi} + \sigma_{\theta r}\cot\theta) + f_r, \tag{41}$$

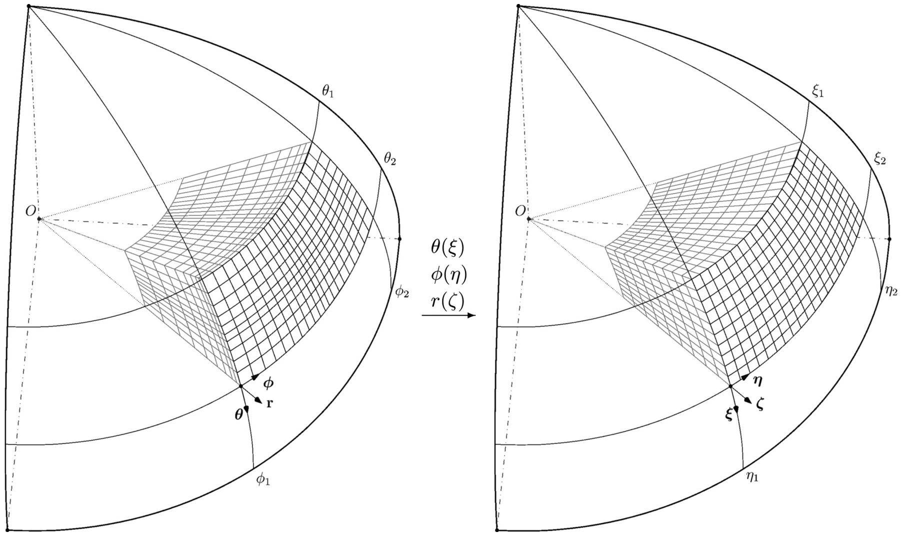

Figure 2. The mapping of the non-uniform grid (left-hand panel) in the physical (θ, ϕ, r) coordinate to a uniform grid (right-hand panel) in the computation (ξ, η, ζ) coordinate.

$$\varepsilon_{\theta\theta,t} = \frac{1}{r}\xi_{,\theta} v_{\theta,\xi} + \frac{1}{r} v_r, \tag{42}$$

$$\varepsilon_{\phi\phi,t} = \frac{1}{r\sin\theta}\eta_{,\phi} v_{\phi,\eta} + \frac{\cot\theta}{r} v_\theta + \frac{1}{r} v_r, \tag{43}$$

$$\varepsilon_{rr,t} = \zeta_{,r} v_{r,\zeta}, \tag{44}$$

$$\varepsilon_{\phi r,t} = \frac{1}{2}\left(\frac{1}{r\sin\theta}\eta_{,\phi} v_{r,\eta} + \zeta_{,r} v_{\phi,\zeta} - \frac{1}{r} v_\phi\right), \tag{45}$$

$$\varepsilon_{\theta r,t} = \frac{1}{2}\left(\frac{1}{r}\xi_{,\theta} v_{r,\xi} + \zeta_{,r} v_{\theta,\zeta} - \frac{1}{r} v_\theta\right), \tag{46}$$

$$\varepsilon_{\theta\phi,t} = \frac{1}{2}\left(\frac{1}{r}\xi_{,\theta} v_{\phi,\xi} + \frac{1}{r\sin\theta}\eta_{,\phi} v_{\theta,\eta} - \frac{\cot\theta}{r} v_\phi\right). \tag{47}$$

The transformed equations on the uniform grid can then be solved without modifying the finite-difference approximation. It turns out that the above transformation is equivalent to replacing the coefficient matrices $\mathbf{A}_\theta$ with $\xi_{,\theta}\mathbf{A}_\theta$, $\mathbf{A}_\phi$ with $\eta_{,\phi}\mathbf{A}_\phi$, and $\mathbf{A}_r$ with $\zeta_{,r}\mathbf{A}_r$ in eq. (22). We use the latter approach for its simpler and easier implementation.

In the aforementioned equations, we need the coefficients of coordinate mapping. Once we know the non-uniform gridpoint locations in spherical coordinates, the physical coordinate derivatives with respect to the reference coordinate can be numerically calculated by using the same finite-difference operator used to solve the wave equations,

$$\theta_{,\xi} = D_\xi \theta, \tag{48}$$

$$\phi_{,\eta} = D_\eta \phi, \tag{49}$$

$$r_{,\zeta} = D_\zeta r, \tag{50}$$

where D is the finite-difference operator. Other partial differential terms will be zero since the grid lines are orthogonal. From the relations,

$$\theta_{,\xi}\,\xi_{,\theta} + \theta_{,\eta}\,\eta_{,\theta} + \theta_{,\zeta}\,\zeta_{,\theta} = 1, \tag{51}$$

$$\theta_{,\xi}\,\xi_{,\phi} + \theta_{,\eta}\,\eta_{,\phi} + \theta_{,\zeta}\,\zeta_{,\phi} = 0, \tag{52}$$

$$\theta_{,\xi}\,\xi_{,r} + \theta_{,\eta}\,\eta_{,r} + \theta_{,\zeta}\,\zeta_{,r} = 0, \tag{53}$$

$$\phi_{,\xi}\,\xi_{,\theta} + \phi_{,\eta}\,\eta_{,\theta} + \phi_{,\zeta}\,\zeta_{,\theta} = 0, \tag{54}$$

$$\phi_{,\xi}\,\xi_{,\phi} + \phi_{,\eta}\,\eta_{,\phi} + \phi_{,\zeta}\,\zeta_{,\phi} = 1, \tag{55}$$

$$\phi_{,\xi}\,\xi_{,r} + \phi_{,\eta}\,\eta_{,r} + \phi_{,\zeta}\,\zeta_{,r} = 0, \tag{56}$$

$$r_{,\xi}\,\xi_{,\theta} + r_{,\eta}\,\eta_{,\theta} + r_{,\zeta}\,\zeta_{,\theta} = 0, \tag{57}$$

$$r_{,\xi}\,\xi_{,\phi} + r_{,\eta}\,\eta_{,\phi} + r_{,\zeta}\,\zeta_{,\phi} = 0, \tag{58}$$

$$r_{,\xi}\,\xi_{,r} + r_{,\eta}\,\eta_{,r} + r_{,\zeta}\,\zeta_{,r} = 1, \tag{59}$$

we can easily derive,

$$\xi_{,\theta} = \frac{1}{\theta_{,\xi}}, \tag{60}$$

$$\eta_{,\phi} = \frac{1}{\phi_{,\eta}}, \tag{61}$$

$$\zeta_{,r} = \frac{1}{r_{,\zeta}}. \tag{62}$$

5 FREE SURFACE BOUNDARY CONDITION

At the free surface, the seismic wave satisfies the traction-free condition,

$$\boldsymbol{\sigma}(R, t) \cdot \hat{\mathbf{n}}|_{r=R} = 0, \tag{63}$$

which is equivalent to the stress-free condition when a perfect spherical Earth is assumed,

$$\sigma_{rr} = 0, \quad \sigma_{\phi r} = 0, \quad \sigma_{\theta r} = 0. \tag{64}$$

Because the stress components and velocity components are related through the stress–strain relation and strain tensor, the stress-free condition also leads to a constraint on the derivatives of the velocity components at the free surface,

$$\mathbf{A}_{\xi}\mathbf{v}_{,\xi} + \mathbf{A}_{\eta}\mathbf{v}_{,\eta} + \mathbf{A}_{\zeta}\mathbf{v}_{,\zeta} + \bar{\mathbf{A}}\mathbf{v} = 0 \tag{65}$$

or

$$\mathbf{v}_{,\zeta} = -\mathbf{A}_{\zeta}{}^{-1}\left[\mathbf{A}_{\xi}\mathbf{v}_{,\xi} + \mathbf{A}_{\eta}\mathbf{v}_{,\eta} + \bar{\mathbf{A}}\mathbf{v}\right], \tag{66}$$

where

$$\mathbf{A}_{\xi} = \frac{\xi_{,\theta}}{r}\begin{bmatrix} C_{13} & C_{36} & C_{35} \\ C_{14} & C_{46} & C_{45} \\ C_{15} & C_{56} & C_{55} \end{bmatrix}, \quad \mathbf{A}_{\eta} = \frac{\eta_{,\phi}}{r\sin\theta}\begin{bmatrix} C_{36} & C_{23} & C_{34} \\ C_{46} & C_{24} & C_{44} \\ C_{56} & C_{25} & C_{45} \end{bmatrix}, \tag{67}$$

$$\mathbf{A}_{\zeta} = \zeta_{,r}\begin{bmatrix} C_{35} & C_{34} & C_{23} \\ C_{45} & C_{44} & C_{34} \\ C_{55} & C_{45} & C_{35} \end{bmatrix}, \quad \bar{\mathbf{A}} = \frac{1}{r}\begin{bmatrix} \cot\theta\, C_{23} - C_{35} & -C_{34} - \cot\theta\, C_{36} & C_{13} + C_{23} \\ \cot\theta\, C_{24} - C_{45} & -C_{44} - \cot\theta\, C_{36} & C_{14} + C_{24} \\ \cot\theta\, C_{25} - C_{55} & -C_{45} - \cot\theta\, C_{56} & C_{15} + C_{25} \end{bmatrix}. \tag{68}$$

The aforementioned matrices can be calculated on the fly at each time step, or calculated once at the beginning of the calculation and saved into memory. The latter approach needs three $27 \times n_i \times n_j$ arrays to store the inversion of $\mathbf{A}_{\zeta}$ multiplied with $\mathbf{A}_{\xi}$, $\mathbf{A}_{\eta}$ and $\bar{\mathbf{A}}$. Alternatively, we

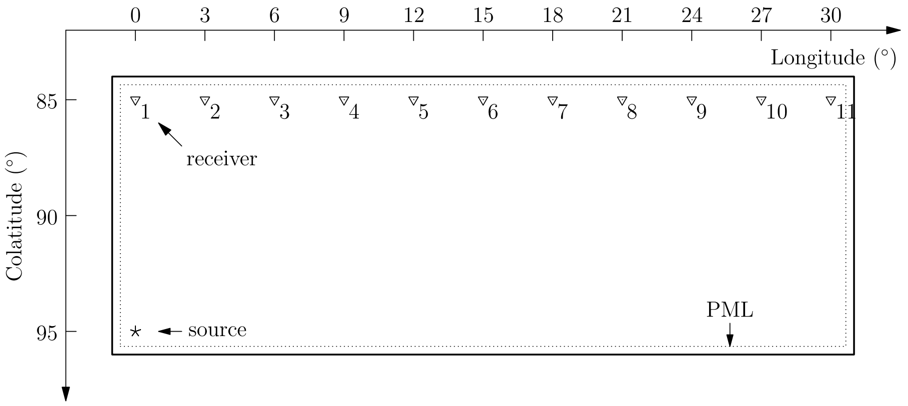

Figure 3. Model range and the source-receiver geometry. Dashed line represents the PML boundary with 12-layer distance to the model boundary. The star symbol indicates the location of the epicentre. There are a total of 11 receivers (inverted triangles) deployed every 3° along the longitude from 0° to 30°E with the same colatitude 85°.

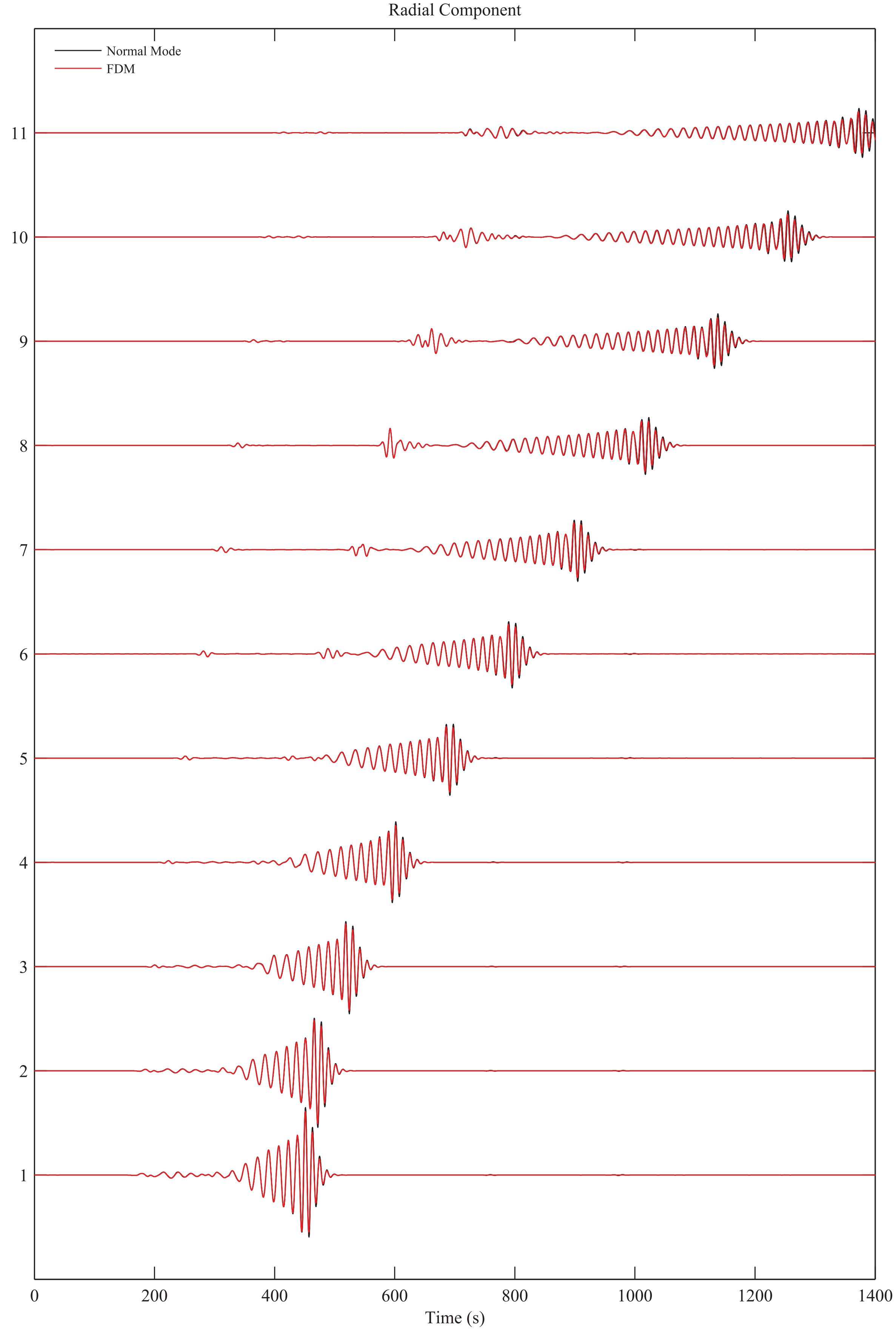

Figure 4. Comparison of the radial component at all the 11 stations between FDM and normal mode in the isotropic PREM.

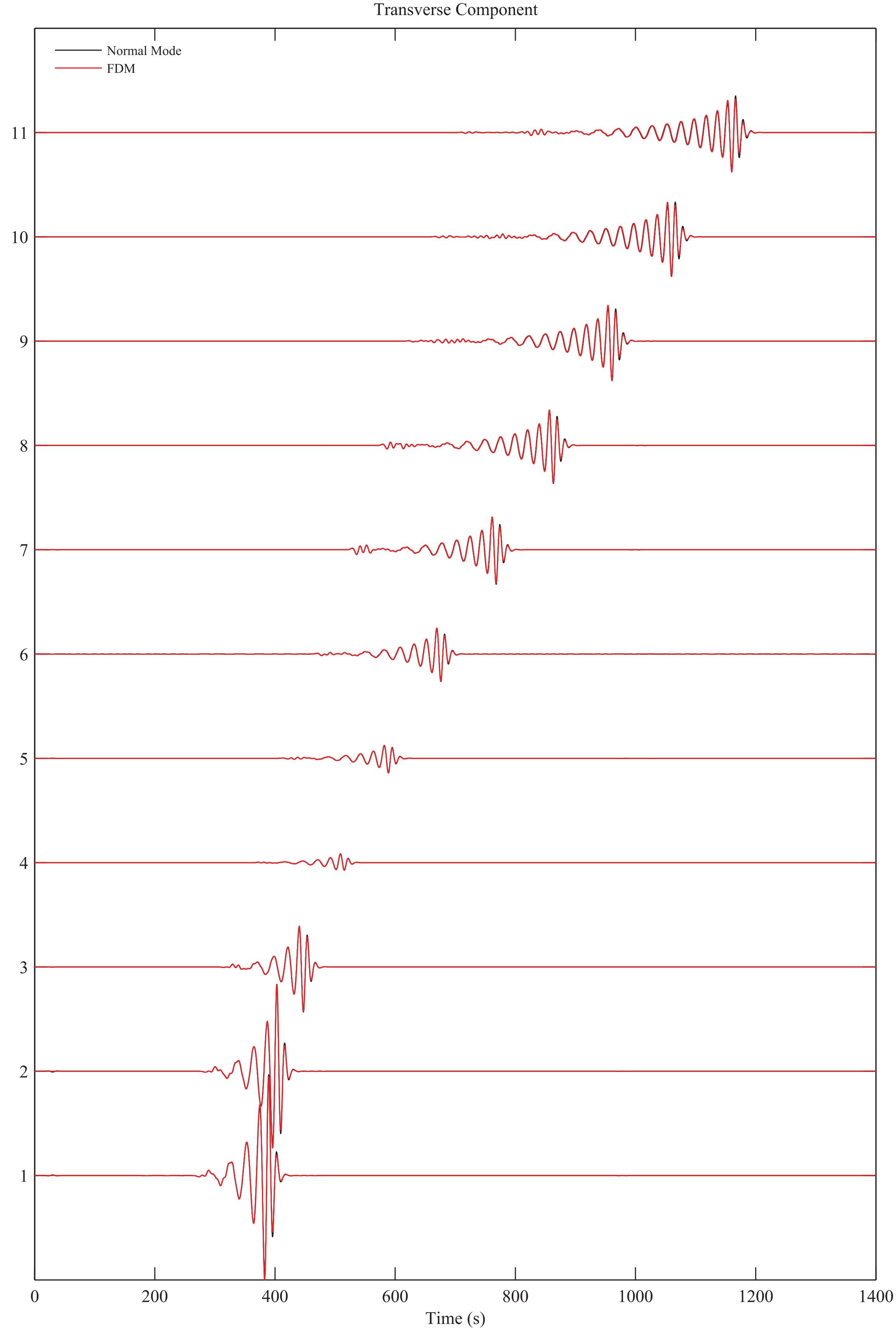

Figure 5. Comparison of the transverse component at all the 11 stations between FDM and normal mode in the isotropic PREM.

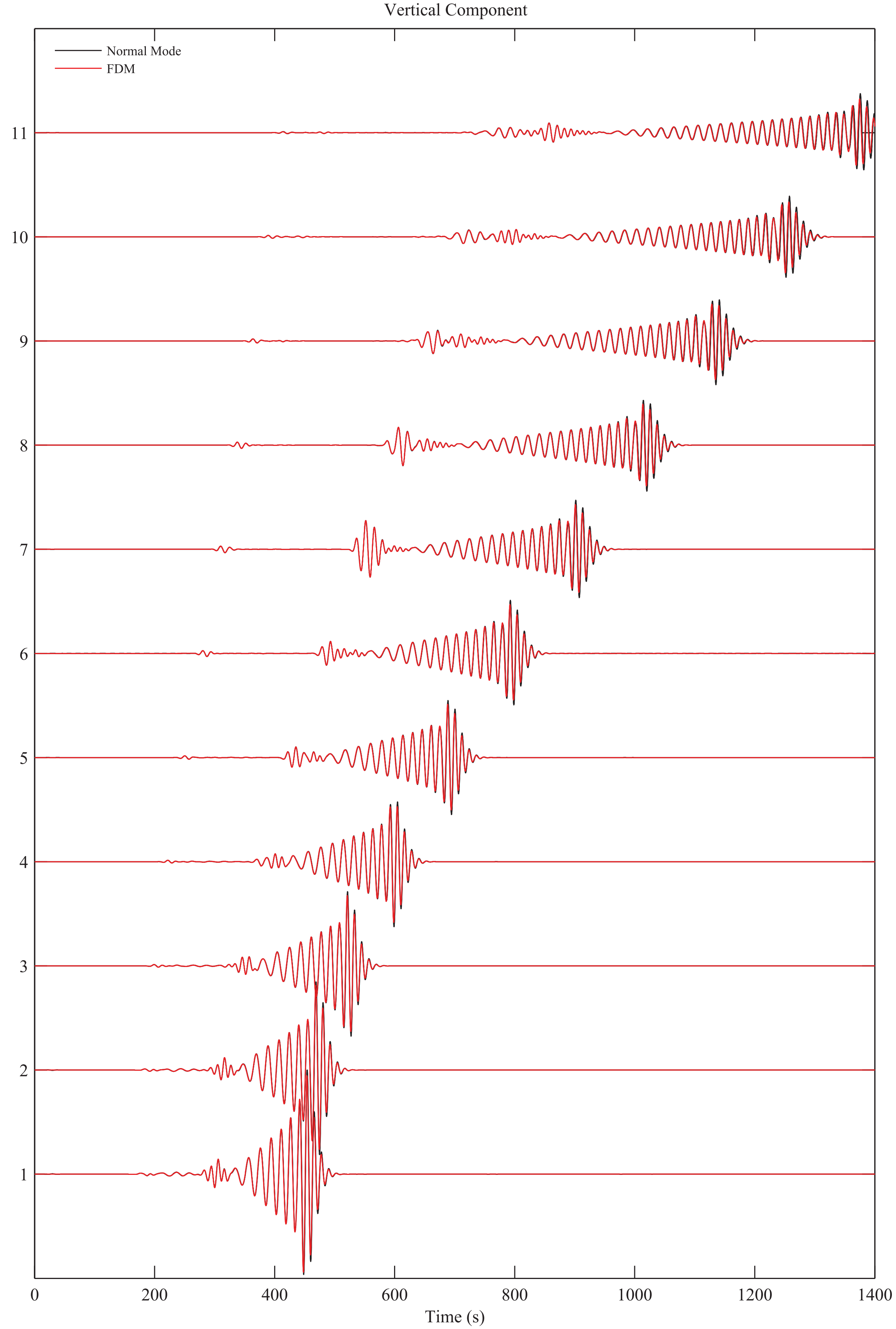

Figure 6. Comparison of the vertical component at all the 11 stations between FDM and normal mode in the isotropic PREM.

can calculate the strain tensor that involves radial derivatives from strain tensors that only involves colatitude and longitude derivatives,

$$\begin{bmatrix} C_{33} & 2C_{34} & 2C_{35} \\ C_{34} & 2C_{44} & 2C_{45} \\ C_{35} & 2C_{45} & 2C_{55} \end{bmatrix} \begin{bmatrix} \varepsilon_{rr,t} \\ \varepsilon_{\phi r,t} \\ \varepsilon_{\theta r,t} \end{bmatrix} + \begin{bmatrix} C_{13} & C_{23} & 2C_{36} \\ C_{14} & C_{24} & 2C_{46} \\ C_{15} & C_{25} & 2C_{56} \end{bmatrix} \begin{bmatrix} \varepsilon_{\theta\theta,t} \\ \varepsilon_{\phi\phi,t} \\ \varepsilon_{\theta\phi,t} \end{bmatrix} = 0, \tag{69}$$

which only need $9 \times n_i \times n_j$ arrays.

The free surface condition on stress components can be easily implemented by stress-image method (Levander 1988; Graves 1996), which antisymmetrically sets value of the stress components at ghost points above the free surface. For free surface boundary condition on velocity components, the derivatives condition (eq. 66) only provides the velocity derivative along r direction on points exactly at the surface, but doesn't provide enough information to completely set the velocity values at ghost points. There are several approaches to deal with this problem: Graves (1996) used a lower-order operator to expand the velocity derivatives at the grid one point above and below the surface to set the velocity values on ghost points. Robertsson (1996) simply set velocity to be zero on ghost points. Rodrigues & Mora (1993) used a lower-order scheme at points near the surface, thus the velocity value on ghost points is not needed. Kristek *et al.* (2002) used an adjusted FD approximations (AFDA) method, in which one side FD operators and compact FD operators are used. Zhang & Chen (2006, 2011) used a compact FD operator of higher-order accuracy near the surface. In this paper, we use the compact FD operators for most cases. If a strong velocity gradient near surface exits, we use a lower-order FD operator to stabilize the simulation.

6 UNSPLIT-FIELD COMPLEX FREQUENCY SHIFT PERFECT MATCHED LAYER

PML (Berenger 1994) is an efficient technique to absorb waves surrounding the computational domain. However, it can generate large spurious reflections for near-grazing incident waves, low frequency waves or evanescent waves (Festa & Vilotte 2005; Drossaert & Giannopoulos 2007b; Komatitsch & Martin 2007). The complex frequency shifted PML (CFS-PML; Kuzuoglu & Mittra 1996) is more effective in such circumstances using a frequency-dependent damping (Festa & Vilotte 2005; Festa *et al.* 2005; Drossaert & Giannopoulos 2007a,b; Komatitsch & Martin 2007). Zhang & Shen (2010) introduced an auxiliary differential equation (ADE) implementation of CFS-PML in the FDTD method in the Cartesian coordinate. We implement this ADE CFS-PML in spherical coordinates based on a spherical-local Cartesian coordinate mapping. Details of this implementation is beyond the scope of this paper.

7 NUMERICAL VERIFICATION

To verify the collocated-grid finite-difference seismic wave modelling in spherical coordinates, we present comparisons of the results from our FDM and those from normal-mode summation (Yang *et al.* 2010) in two sets of numerical tests. The first test is performed in the isotropic continental PREM, and the second test uses the anisotropic continental PREM.

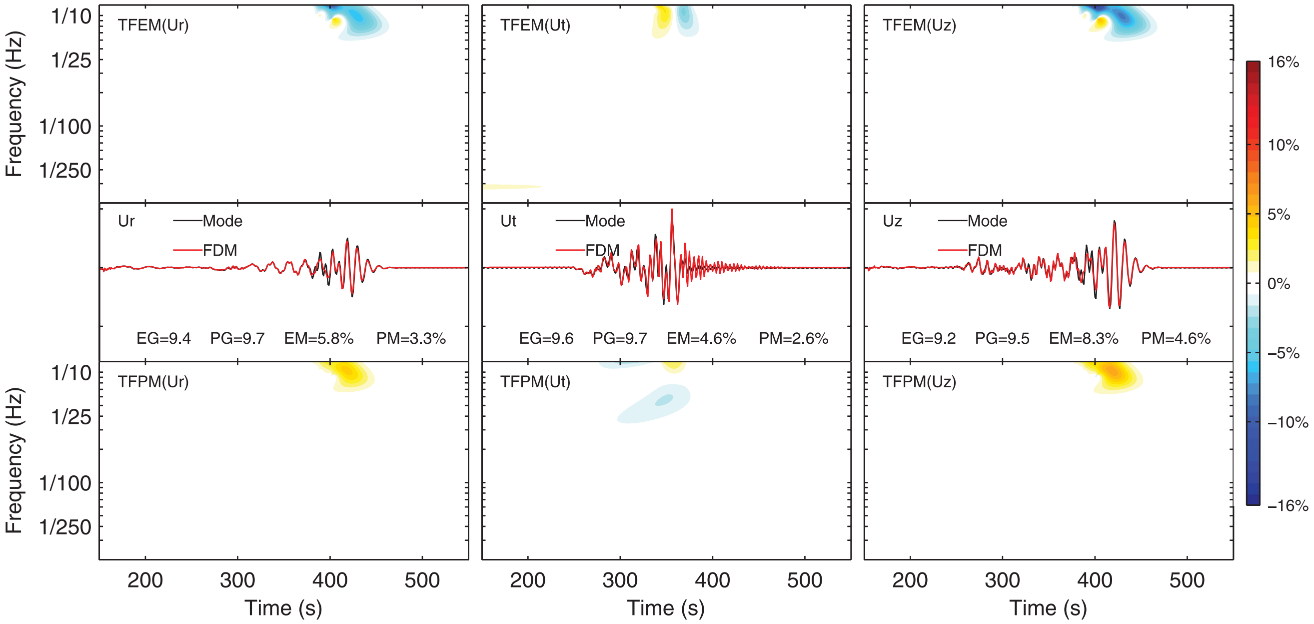

Figure 7. Time-frequency envelop misfit (TFEM; top row) and phase misfit (TFPM, bottom row) between the FDM solutions (dash–dotted red line, middle row) and the reference normal mode solutions (solid black line, middle row) at receiver 1 for the isotropic PREM and a step source time function. Left-hand column: radial component. Middle column: transverse component. Right-hand column: vertical component. Values of the single-valued envelop goodness-of-fit (EG), phase goodness-of-fit (PG), envelop misfit (EM) and phase misfit (PM) are labelled in the middle row.

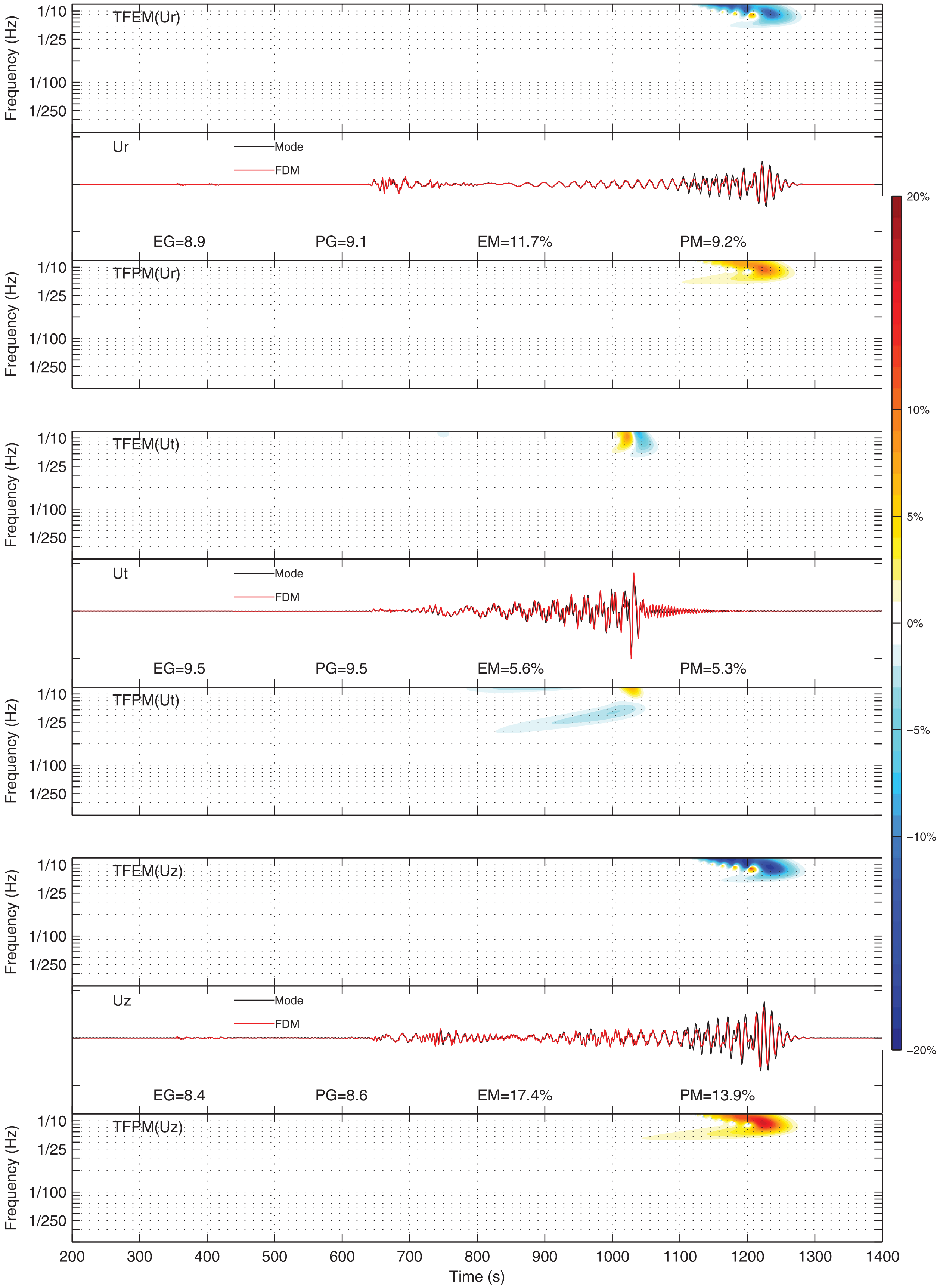

Figure 8. Time-frequency envelop misfit (TFEM) and phase misfit (TFPM) between the FDM solutions (red colour) and the reference normal mode solutions (black colour) at receiver 10 for the isotropic PREM and a step source time function. Values of the single-valued envelop goodness-of-fit (EG), phase goodness-of-fit (PG), envelop misfit (EM) and phase misfit (PM) are also labelled.

The two tests share the same source-receiver configuration. Fig. 3 shows the model range and the source–receiver geometry. The computational domain covers 32° along longitude (−1° to 31°E) and 12° along colatitude (84°–96°) with 34 finite-difference nodes per degree. Thus, the horizontal grid spacing is roughly 3.2 km at the surface. A non-uniform grid covers 903 km along the radial direction (from 5468 to 6371 km at the surface), with a grid spacing that gradually increases from 1 km near the surface to around 6 km at 800 km depth. There are 12 PML layers surrounding the model boundaries except the free surface. The model size is 31.3° × 11.3° × 833 km excluding the PML layers. A double couple source (strike = 45°, dip = 45° and rake = 90°) is located at colatitude = 95°, longitude = 0° and depth = 20 km. Both simulations are carried out using four quad-core (two AMD Opteron 2218 dual-core CPU) nodes. Comparing to the isotropic case, the anisotropy has a negligible affect on computational efficiency. Both simulations need nearly the same computational time, around 25 hr each. The anisotropic case needs a little more memory than the isotropic case, around 1220 MB/thread versus 1130 MB/thread.

7.1 Comparison with normal mode method for isotropic continental PREM

In the first numerical test, we use a modified isotropic PREM, in which the ocean water is replaced by the upper crust material. In Section 8, we discuss the effects of the ocean layer on the simulation results. Figs 4–6 show the comparison of the displacement at the 11 receivers

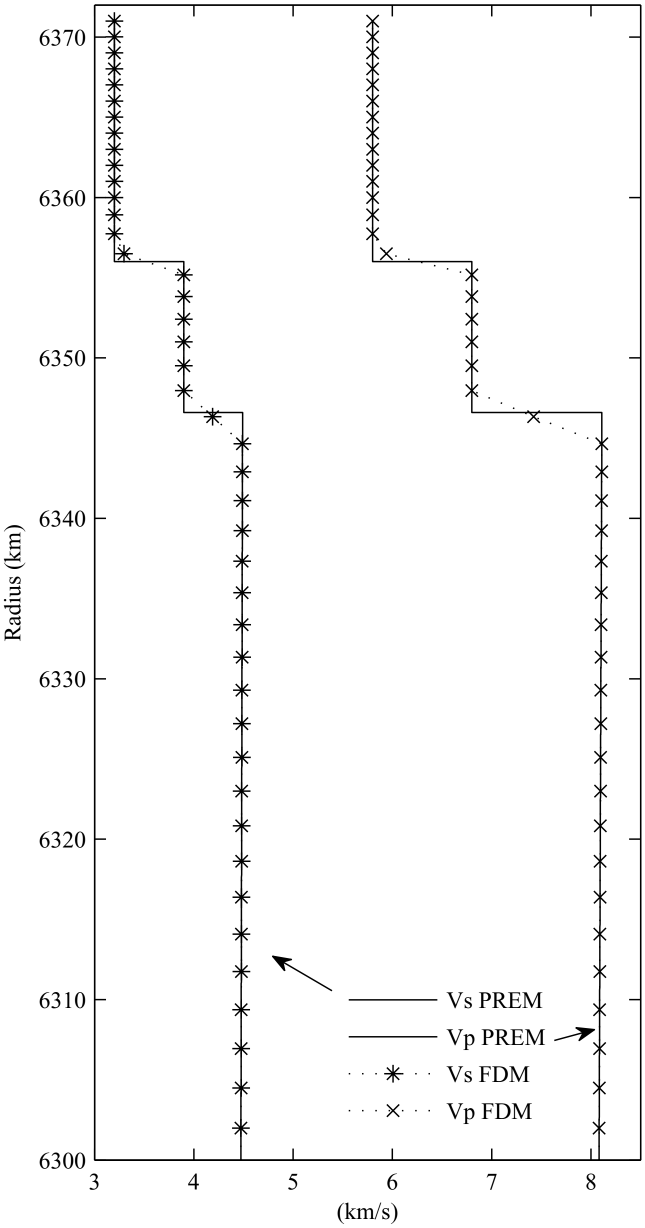

Figure 9. Comparison of the velocity profile on FDM grid and for the normal mode for the isotropic PREM above 6300 km.

between the normal mode method and FDM for the radial, transverse and vertical components, respectively. We do not observe high frequency grid-to-grid oscillation in the FDM solutions. The overall patterns of the waveforms are well matched between the normal mode method and FDM for all the 11 receivers. The direct body phases (*P* and *S* waves) and the early surface phase are matched very well in all the three components. The amplitude of the surface wave coda shows some discrepancies. Because surface wave coda has a higher frequency and the surface wave has a shorter wavelength compared to body phases of the same frequency, it needs smaller grid size to achieve the same accuracy as body phases. In this numerical test, the source time function is the Ricker wavelet with a centre frequency of 0.05 Hz. Therefore, the maximum frequency of the source is around 0.125 Hz (2.5 times the centre frequency), corresponding to the shortest period of 8 s. The minimal *S*-wave speed is 3.2 km s^{-1}. Thus, the points per shortest wavelength (PPW) for *S* wave is around eight.

To further quantitatively assess the agreement between the two methods both in time and frequency domains, we calculate the time-frequency (TF) misfit and goodness-of-fit measurement, developed in Kristekova *et al.* (2006) and Kristekova *et al.* (2009a), of the FDM solutions and the normal mode solutions. The TF misfit criteria and the goodness-of-fit criteria are calculated from the TF representation of the signals using the continuous wavelet transform. The benefit of the TF representation is that it can separate the envelope (amplitude) misfit and the phase misfit, and provide the misfit information both in time domain and frequency domain simultaneously. Since the TF goodness-of-fit criteria are most suitable in the case of large differences between two signals (Kristekova *et al.* 2009a), in the following, we mainly present

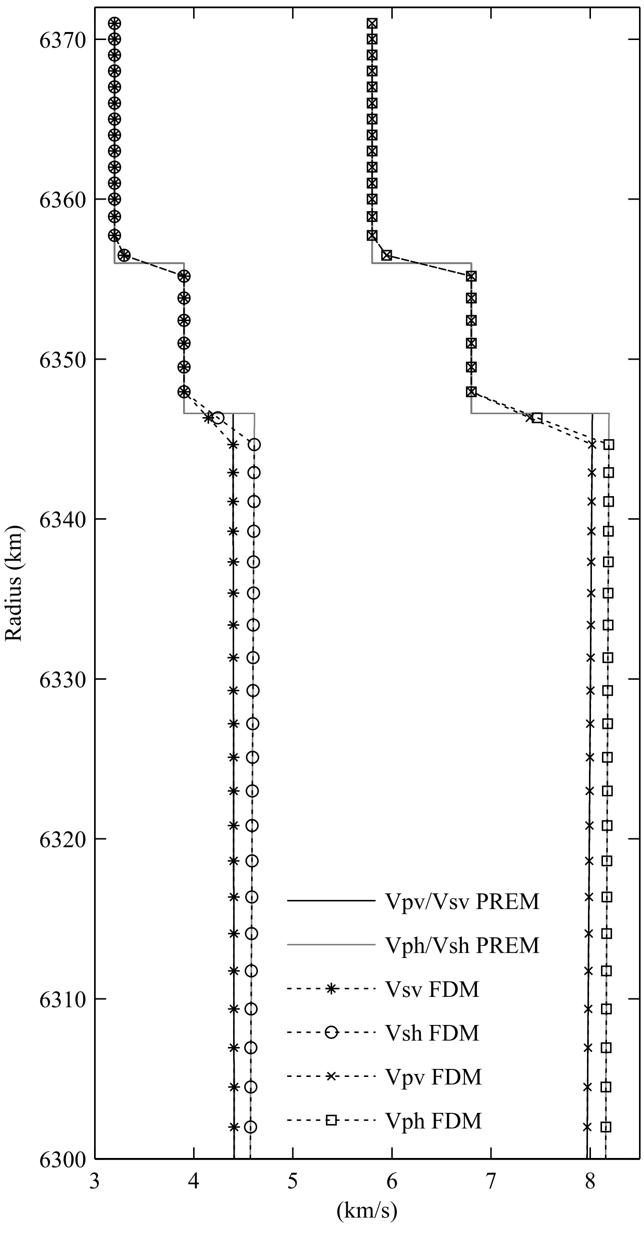

Figure 10. Comparison of the velocity profile on FDM grid and for the normal mode for the anisotropic PREM above 6300 km.

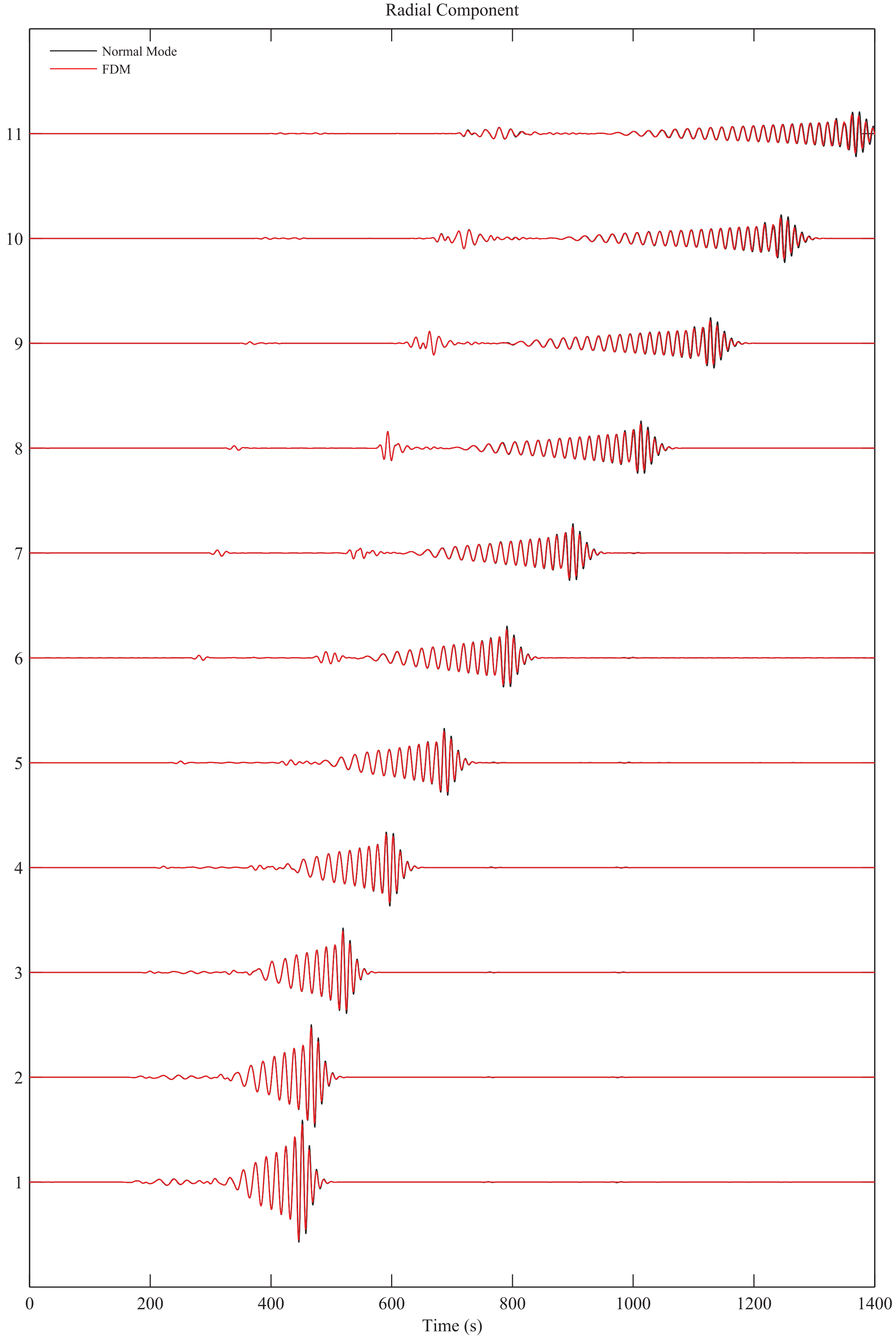

Figure 11. Comparison of the radial component at all the 11 stations between FDM and normal mode in the anisotropic PREM.

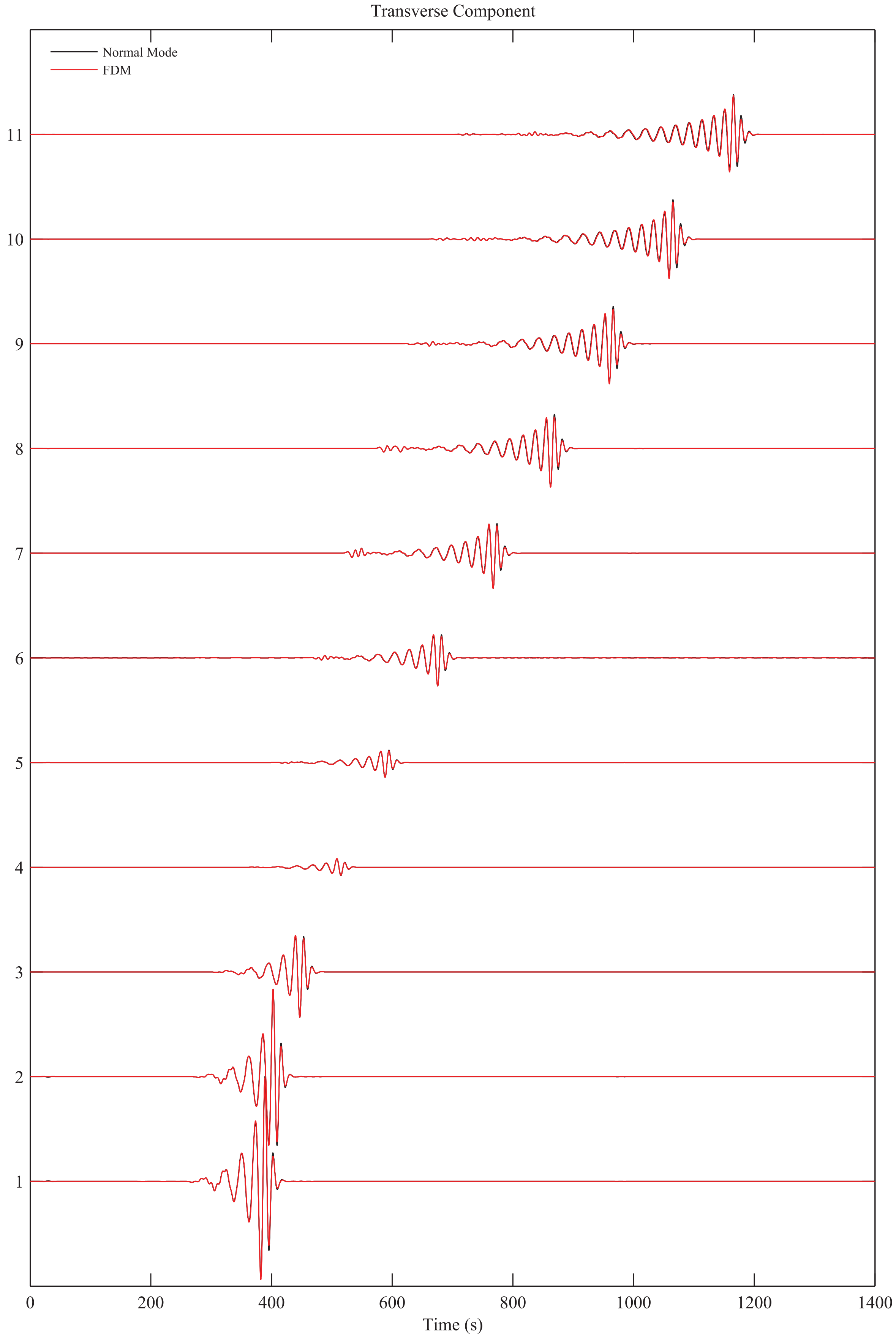

Figure 12. Comparison of the transverse component at all the 11 stations between FDM and normal mode in the anisotropic PREM.

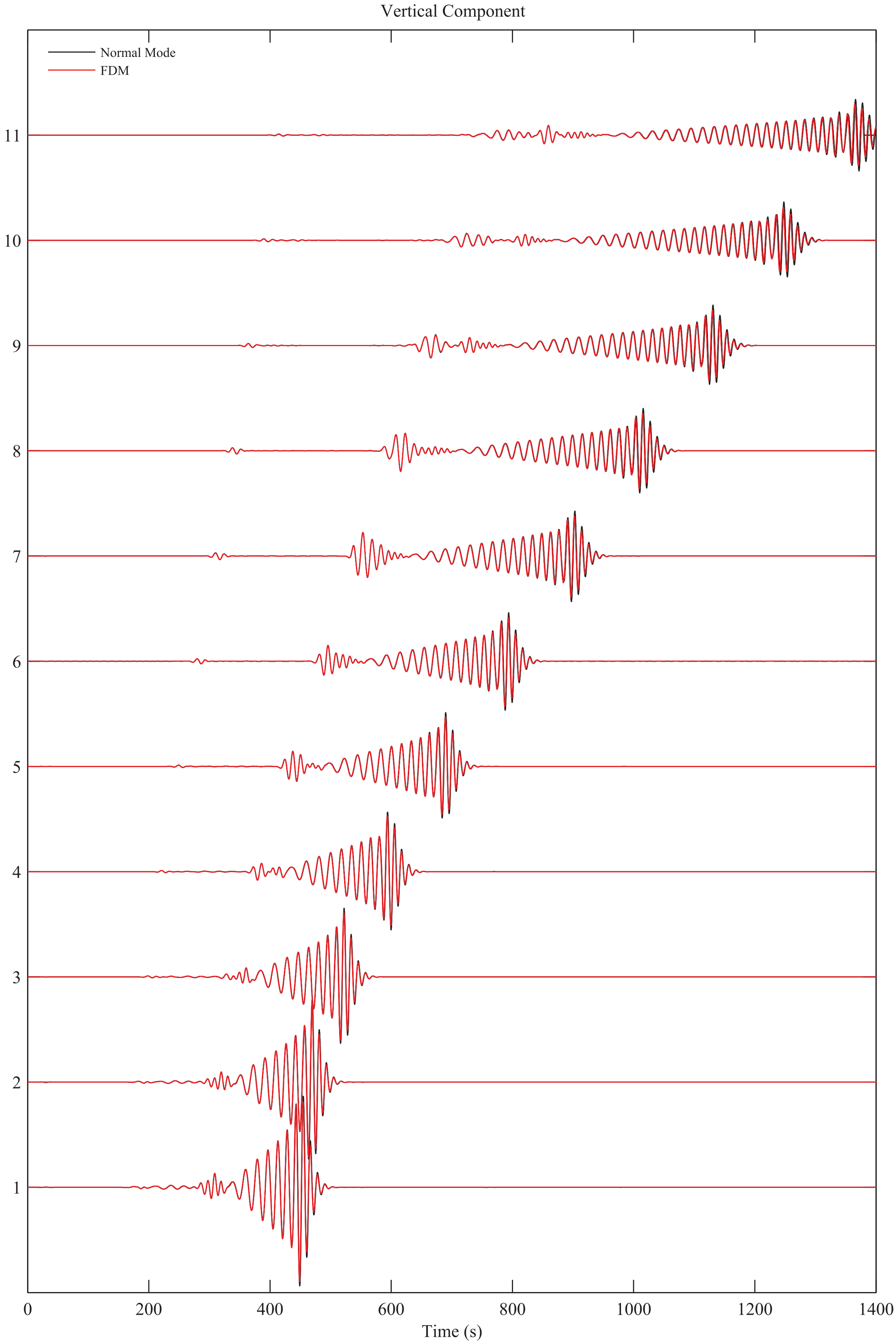

Figure 13. Comparison of the vertical component at all the 11 stations between FDM and normal mode in the anisotropic PREM.

the TF envelop misfit (TFEM) and phase misfit (TFPM) comparisons. We also show the global measurements of the agreement between the two solutions: single-valued envelop misfit (EM), phase misfit (PM), envelop goodness-of-fit (EG) and phase goodness-of-fit (PG). All these values are calculated using the TF_MISFIT_GOF_CRITERIA package (Kristekova *et al.* 2009b).

For a better representation of the TF misfit at all frequencies, we replace the Ricker wavelet with a step function as the source time function in both the normal mode method and FDM, since the frequency amplitude of the Ricker wavelet is not flat with respect to frequency and decays both sides around the centre frequency. We use receiver 1 and receiver 10 as the representatives. Fig. 7 shows the TF misfit and goodness-of-fit at receiver 1. Because the step function contains frequencies higher than the grid can resolve (0.125 Hz for S wave in this test), the waveform difference becomes notable in Fig. 7. However, at frequencies below 0.125 Hz, all the body phases fit very well. The errors happen in the surface wave window and at high frequencies, because the surface wave has a shorter wavelength than body phases and needs more PPW than body phases to achieve accurate simulation. The error in amplitude is relatively larger than the error in phase. The DRP/opt MacCormack scheme has inherent dissipation to suppress the odd-even decoupling mode on the collocated grid. The relatively larger error in amplitude than in phase is attributed to this numerical dissipation. Fig. 8 shows the TF misfit and goodness-of-fit at receiver 10, which shows similar patterns as Fig. 7.

The TF misfit measurement separates signal misfits at different frequencies, but it could be easily understood through commonly used measurements. For example, the TFPM on the vertical component in Fig. 7 is around 5 per cent at 0.1 Hz, which is equivalent to a 0.5 s delay for a cross-correlation measurement of the 10 s period wave between the 400 and 420 s time window.

It is worth noting that the vertical grid used in this test does not align with the inner discontinuities (Fig. 9). We use the volume averaged effective media parameters approach (Moczo *et al.* 2002) to account for the inner discontinuities. The fit between the normal mode method and FDM demonstrates that the spherical FDM can deal with arbitrary complex media.

7.2 Comparison with the normal mode method for the solid anisotropic PREM

In this numerical test, we use a modified anisotropic PREM, in which the ocean water is replaced by the upper crust material. The source time functions are the same as in the corresponding calculations in the isotropic PREM.

Fig. 10 shows the anisotropic velocity profiles on the finite-difference nodes. For anisotropic media, the values of the stiffness components on the finite-difference nodes are derived using harmonic volume averaging as for the elastic moduli in Moczo *et al.* (2002).

Figs 11–13 show the comparison of the displacement at the 11 receivers between the normal mode method and FDM for the radial, transverse and vertical components, respectively. The collocated-grid finite-difference scheme is well suited to handle anisotropy media since all the stress components are at the same grid position. The waveform comparisons for all the three components at all the 11 receivers show a similar good agreement between the normal mode method and FDM. The direct body phases (P and S wave) and the early surface phase are matched very well, while the amplitude of the later surface wave shows some discrepancies.

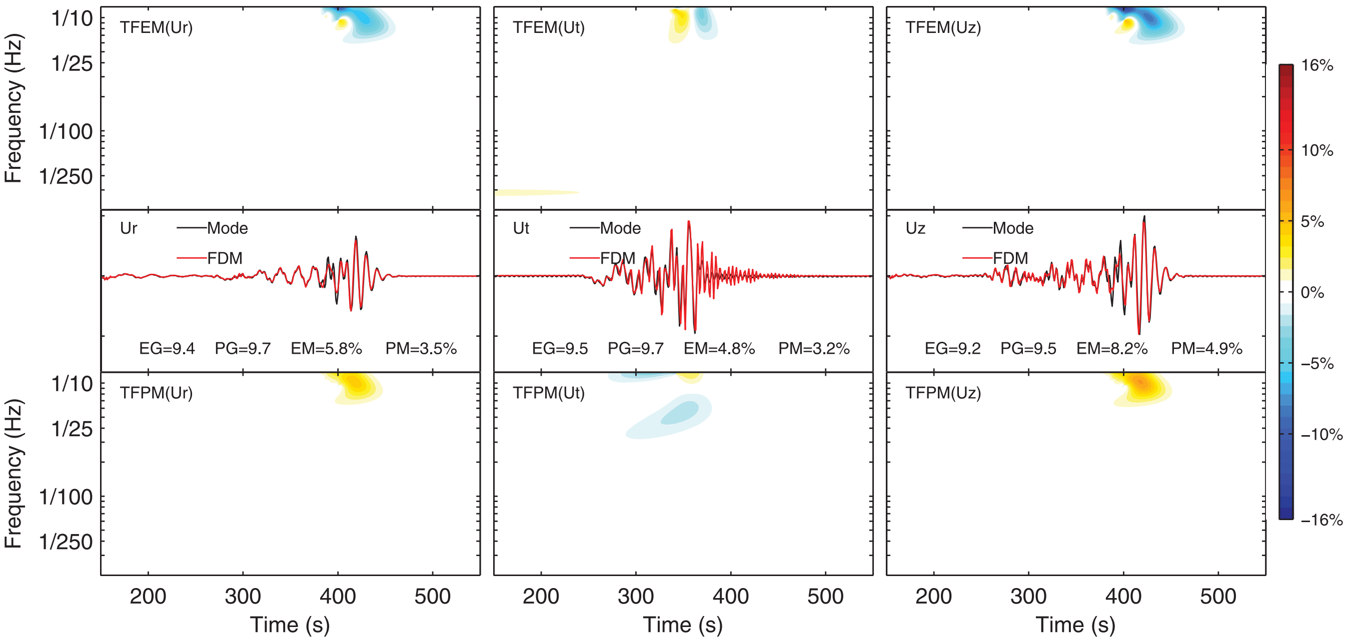

Figure 14. Time-frequency envelop misfit (TFEM; top row) and phase misfit (TFPM, bottom row) between the FDM solutions (dash-dotted red line, middle row) and the reference normal mode solutions (solid black line, middle row) at receiver 1 for the anisotropic PREM and a step source time function. Left column: north component. Middle column: east component. Right column: vertical component. Values of the single-valued envelop goodness-of-fit (EG), phase goodness-of-fit (PG), envelop misfit (EM) and phase misfit (PM) are labelled in the middle row.

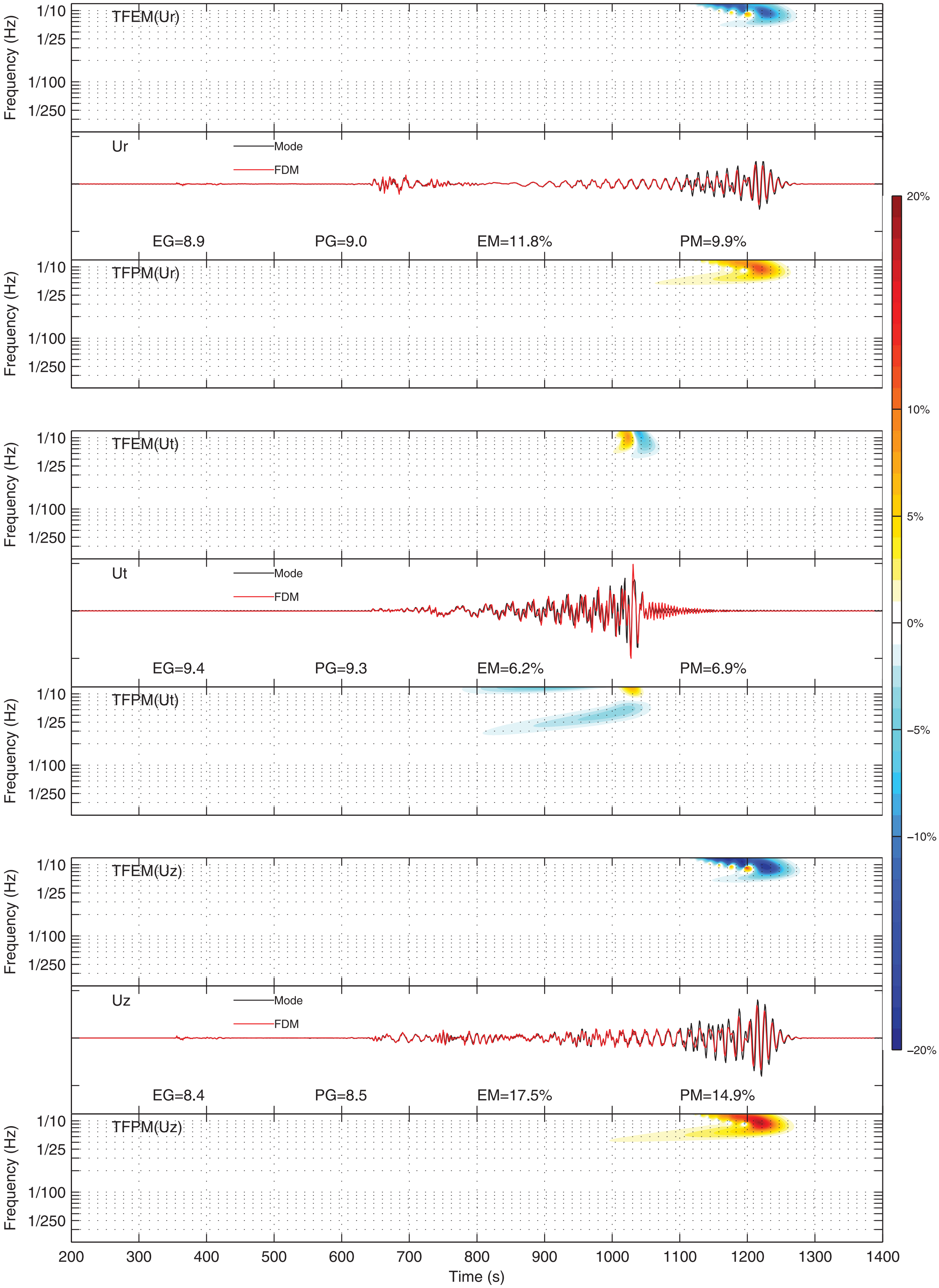

Figure 15. Time-frequency envelop misfit (TFEM) and phase misfit (TFPM) between the FDM solutions (red colour) and the reference normal mode solutions (black colour) at receiver 10 for the anisotropic PREM and a step source time function. Values of the single-valued envelop goodness-of-fit (EG), phase goodness-of-fit (PG), envelop misfit (EM) and phase misfit (PM) are also labelled.

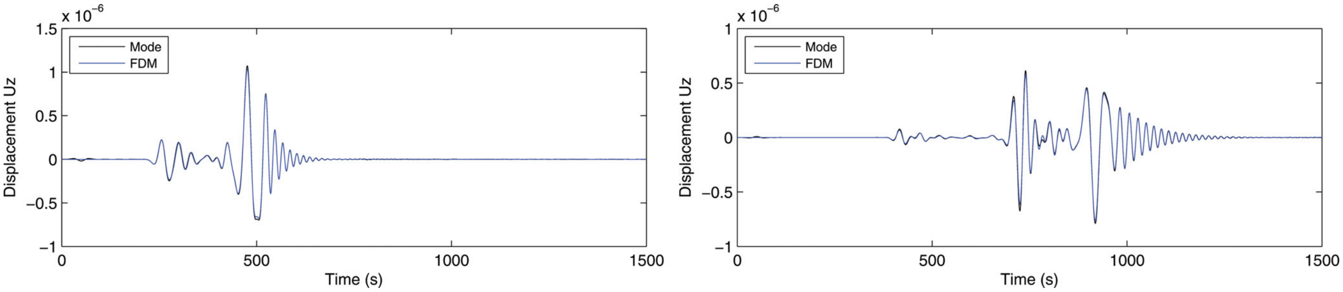

Figure 16. Comparison of the vertical component at 15° (left-hand panel) and 30° (right-hand panel) from FDM and normal mode in the anisotropic PREM with 3 km ocean layer. Because the water layer is thin, the vertical grid spacing in the ocean layer is 500 m. The horizonal grid spacing is still around 3.2 km. The centre frequency of the source (the Ricker wavelet) is 0.02 Hz.

The TF misfit at receiver 1 for the anisotropic PREM (Fig. 14) are very similar to the results for the isotropic PREM (Fig. 7). The TF misfit at receiver 10 for the anisotropic PREM (Fig. 15) also shows a similar pattern as Fig. 8.

8 DISCUSSION AND CONCLUSION

The north and south poles and the centre of the Earth are singularities for seismic wave modelling in spherical coordinates. If the target area includes or is close to the north or south pole, we can use a 3-D spherical rotation to centre the target area around the equator. Such rotation also helps to minimize the difference in the grid size and improve computational efficiency (Igel *et al.* 2002). To include the centre of the Earth in simulation, one can incorporate the discontinuous grid (Kristek *et al.* 2010) to improve computational efficiency and extend the model to the deepest earth. This is beyond the scope of this paper.

It is straightforward to include the ocean layer in our collocated-grid finite-difference scheme. This is achieved by setting $\mu = 0$ in the water layer, as demonstrated in Fig. 16, which shows a comparison of the FDM and normal model results for the anisotropic PREM that includes a 3-km-thick ocean layer. In this paper, we use an optimized, collocated-grid finite-difference scheme, the DRP/opt MacCormack scheme, to solve the velocity–stress equation in spherical coordinates. In the DRP/opt MacCormack scheme, all the variables are at the same location in a gridpoint, thus it is straightforward to account for the Earth's anisotropy in the simulation. To reduce the memory requirement, we only use five independent parameters if the anisotropy exhibits a radial symmetry. We use all 21 parameters for other anisotropic media.

To increase the efficiency of the finite-difference algorithm, we use a grid with non-uniform grid spacing to discretize the computational domain. The grid varies continuously with smaller spacing in low velocity layers and thin layer regions and with larger spacing otherwise.

We use stress-image setting to implement the free surface boundary condition on the stress components. To implement the free surface boundary condition on the velocity components, we use a compact scheme near the surface. If a strong velocity gradient exists near the surface, a lower-order scheme is used to calculate velocity difference to stabilize the calculation. The computational domain is surrounded by complex-frequency shifted PMLs implemented through auxiliary differential equations in a local Cartesian coordinate.

We compare the FDM simulation results with the results from the normal mode method in the isotropic and anisotropic PREM and verify the accuracy of the FDM scheme. With TF misfit measurements, we demonstrate the excellent fit of body waves and longer period surface waves. The error in short period surface waves is attributed to the fact that surface waves need more points per shortest wavelength than body phases to achieve the same accurate simulation. TF misfit measurements like in Figs 7 and 8 provide a quantitative basis to determine the required grid sizes for a given frequency wave and acceptable computational error or the shortest usable period wave for a given grid size in application.

ACKNOWLEDGMENTS

We are grateful to Daniel Peter and another anonymous reviewer for their constructive comments. This research was supported by in part by the USA National Science Foundation under awards EAR-0551117 and EAR-0738779 and the USA Air Force Research Laboratory under award FA9453-10-C-0217.

REFERENCES

Bayliss, A., Jordan, K.E., Lemesurier, B.J. & Turkel, E., 1986. A 4th-order accurate finite-difference scheme for the computation of elastic-waves, *Bull. seism. Soc. Am.,* **76,** 1115–1132.

Bérenger, J.P., 1994. A perfectly matched layer for the absorption of electromagnetic waves, *J. Comput. Geophys.,* **114,** 185–200.

Dai, N., Vafidis, A. & Kanasewich, E.R., 1995. Wave-propagation in heterogeneous, porous-media—a velocity-stress, finite-difference method, *Geophysics,* **60,** 327–340.

Drossaert, F.H. & Giannopoulos, A., 2007a. A nonsplit complex frequencyshifted PML based on recursive integration for FDTD modeling of elastic waves, *Geophysics,* **72**(2), T9–T17.

Drossaert, F.H. & Giannopoulos, A., 2007b. Complex frequency shifted convolution PML for FDTD modelling of elastic waves, *Wave Motion,* **44,** 593–604.

Dziewonski, A.M. & Anderson, D.L., 1981. Preliminary reference earth model, *Phys. Earth planet. Inter.,* **25,** 297–356.

Festa, G. & Vilotte, J.P., 2005. The Newmark scheme as velocity-stress time-staggering: an efficient PML implementation for spectral-element simulations of elastodynamics, *Geophys. J. Int.,* **161,** 789–812.

Festa, G., Delavaud, E. & Vilotte, J.P., 2005. Interaction between surface waves and absorbing boundaries for wave propagation in geological basins: 2D numerical simulations, *Geophys. Res. Lett.,* **32,** L20306, doi:10.1029/2005GL024091.

Fichtner, A., 2011. *Full Seismic Waveform Modelling and Inversion,* Springer-Verlag, Heidelberg.

Fichtner, A., Igel, H., Bunge, H.P. & Kennett, B.L.N., 2009a. Simulation and inversion of seismic wave propagation on continental scales based on a spectral-element method, *J. Numer. Anal., Ind. Appl. Math.,* **4**(1–2), 11–22.

Fichtner, A., Kennett, B.L.N., Igel, H. & Bunge, H.P., 2009b. Full seismic waveform tomography for upper-mantle structure in the Australasian region using adjoint methods, *Geophys. J. Int.,* **179**(3), 1703–1725.

Gottlieb, D. & Turkel, E., 1976. Dissipative 2-4 methods for time-dependent problems, *Math. Comput.,* **30,** 703–723.

Graves, R.W., 1996. Simulating seismic wave propagation in 3D elastic media using staggered-grid finite differences, *Bull. seism. Soc. Am.,* **86,** 1091–1106.

Hixon, R., 1997. On increasing the accuracy of MacCormack schemes for aeroacoustic applications, *AIAA Paper,* 97–1586.

Hixon, R. & Turkel, E., 2000. Compact implicit MacCormack-type schemes with high accuracy, *J. Comput. Phys.,* **158,** 51–70.

Igel, H., 1999. Wave propagation in spherical sections using the Chebyshev method, *Geophys. J. Int.,* **136,** 559–567.

Igel, H. & Weber, M., 1995. SH wave propagation in the whole mantle using high-order finite differences, *Geophys. Res. Lett.,* **22,** 731–734.

Igel, H. & Weber, M., 1996. P-SV wave propagation in the Earth's mantle using finite-differences: application to heterogeneous lowermost mantle structure, *Geophys. Res. Lett.,* **23,** 415–418.

Igel, H., Mora, P. & Riollet, B., 1995. Anisotropic wave-propagation through finite-difference grids, *Geophysics,* **60,** 1203–1216.

Igel, H., Nissen-Meyer, T. & Jahnke, G., 2002. Wave propagation in 3-D spherical sections: effects of subduction zones, *Phys. Earth planet. Inter.,* **132,** 219–234.

Jahnke, G., Thorne, M.S., Cochard A. & Igel, H., 2008. Global SH-wave propagation using a parallel axisymmetric spherical finite-difference scheme: application to whole mantle scattering, *Geophys. J. Int.,* **173,** 815–826.

Komatitsch, D. & Martin, R., 2007. An unsplit convolutional Perfectly Matched Layer improved at grazing incidence for the seismic wave equation, *Geophysics,* **72**(5), SM155–SM167.

Komatitsch, D. & Tromp, J., 2002a. Spectral-element simulations of global seismic wave propagation—I. Validation, *Geophys. J. Int.,* **149,** 390–412.

Komatitsch, D. & Tromp, J., 2002b. Spectral-element simulations of global seismic wave propagation—II. 3-D models, oceans, rotation, and self-gravitation, *Geophys. J. Int.,* **150,** 303–318.

Kristek, J., Moczo, P. & Archuleta, R.J., 2002. Efficient methods to simulate planar free surface in the 3D 4(th)-order staggered-grid finite-difference schemes, *Stud. Geophys. Geod.,* **46,** 355–381.

Kristek, J., Moczo, P. & Galis, M., 2010. Stable discontinuous staggered grid in the finite-difference modelling of seismic motion, *Geophys. J. Int.,* **183,** 1401–1407.

Kristekova, M., Kristek, J., Moczo, P. & Day, S.M., 2006. Misfit criteria for quantitative comparison of seismograms, *Bull. seism. Soc. Am.,* **96,** 1836–1850.

Kristekova, M., Kristek, J. & Moczo, P., 2009a. Time-frequency misfit and goodness-of-fit criteria for quantitative comparison of time signals, *Geophys. J. Int.,* **178,** 813–825.

Kristekova, M., Kristek, J. & Moczo, P., 2009b. *Users's Guide to TF_MISFIT_GOF_CRITERIA*, available at: http://www.nuquake.eu/Computer_Codes/ (last accessed 2012 January 7).

Kuzuoglu, M. & Mittra, R., 1996. Frequency dependence of the constitutive parameters of causal perfectly matched anisotropic absorbers, *IEEE Microw. Guided Wave Lett.,* **6,** 447–449.

Levander, A.R., 1988. 4th-order finite-difference p-sv seismograms, *Geophysics,* **53,** 1425–1436.

Love, A.E.H., 1927. *A Treatise on the Mathematical Theory of Elasticity,* 4th edn, Cambridge University Press, Cambridge, 643 pp.

MacCormack, R.W., 1969. The effect of viscosity in hypervelocity impact cratering, *AIAA Paper,* 69–354.

Madariaga, R., 1976. Dynamics of an expanding circular fault, *Bull. seism. Soc. Am.,* **66,** 639–666.

Magnier, S.A., Mora, P. & Tarantola, A., 1994. differences on minimal grids, *Geophysics,* **59**(9), 1435–1443.

Moczo, P., Kristek, J., Vavrycuk, V., Archuleta, R.J. & Ladislav, H., 2002. 3D heterogeneous staggered-grid finite-difference modeling of seismic motion with volume harmonic and arithmetic averaging of elastic moduli and densities, *Bull. seism. Soc. Am.,* **92,** 3042–3066.

Nissen-Meyer, T., 2001. *Numerical Simulation of Seismic Wave Propagation through Subduction Zones*. Ludwig-Maximilians-University Munich, Germany.

Nissen-Meyer, T., Fournier, A. & Dahlen, F.A., 2006. A 2-D spectral-element method for computing spherical-Earth seismograms—I. Moment-tensor source, *Geophys. J. Int.,* **168,** 1067–1092, doi:10.1111/j.1365-246X.2006.03121.x.

Patankar, S., 1980. *Numerical Heat Transfer and Fluid Flow*. McGraw-Hill, New York.

Pitarka, A., 1999. 3D elastic finite-difference modeling of seismic motion using staggered grids with nonuniform spacing, *Bull. seism. Soc. Am,* **89**(1), 54–68.

Robertsson, J., 1996. A numerical free-surface condition for elastic/viscoelastic finite-difference modeling in the presence of topography, *Geophysics,* **61,** 1921–1934.

Rodrigues, D. & Mora, P., 1993. An efficient implementation of the free-surface boundary condition in 2-D and 3-D elastic cases, *SEG Expanded Abstracts,* **12,** 215–217.

Tam, C. & Webb, J.C., 1993. Dispersion-relation-preserving finite-difference schemes for computational acoustics, *J. Comput. Phys.,* **107,** 262–281.

Tsingas, C., Vafidis, A. & Kanasewich, E.R., 1990. Elastic wave-propagation in transversely isotropic media using finite-differences, *Geophys. Prospect.,* **38,** 933–949.

Vafidis, A., Abramovici, F. & Kanasewich, E.R., 1992. Elastic wave-propagation using fully vectorized high-order finite-difference algorithms, *Geophysics,* **57**(2), 218–232.

Virieux, J., 1984. SH-wave propagation in heterogeneous media - velocity-stress finite-difference method, *Geophysics,* **49,** 1933–1942.

Virieux, J., 1986. P-SV-wave propagation in heterogeneous media—velocity-stress finite-difference method, *Geophysics,* **51,** 889–901.

Wang, Y.B., Takenaka, H. & Furumura, T., 2001. Modelling seismic wave propagation in a two-dimensional cylindrical whole-earth model using the pseudospectral method, *Geophys. J. Int.,* **145,** 689–708.

Xie, X.B. & Yao, Z.X., 1988. P-SV wave responses for a point source in two-dimensional heterogeneous media: finite-difference approximation, *Chi. J. Geophys.,* **31**(3), 473–493.

Yang, H.-Y., Zhao, L. & Hung, S.-H., 2010. Synthetic seismograms by normal-mode summation: a new derivation and numerical examples, *Geophys. J. Int.,* **183,** 1613–1632.

Zahradnik, J., 1995. Simple elastic finite-difference scheme, *Bull. seism. Soc. Am.,* **85,** 1879–1887.

Zhang, W. & Chen, X.F., 2006. Traction image method for irregular free surface boundaries in finite difference seismic wave simulation, *Geophys. J. Int.,* **167,** 337–353.

Zhang, W. & Shen, Y., 2010. Unsplit complex frequency-shifted PML implementation using auxiliary differential equation for seismic wave modeling, *Geophysics,* **75,** T141–T154.

Zhang, W., Shen, Y. & Chen, X.F., 2008. Numerical simulation of strong ground motion for the M (s) 8.0 Wenchuan earthquake of 12 May 2008, *Sci.China,* **51**(12), 1673–1682.

Zhang, W., Chen, X.F. & Zhang, Z.G., 2011. 3-D elastic wave numerical modeling in the presence of surface topography by a collocated-grid finite difference method on curvilinear grid, *Geophys. J. Int*. submitted

Zhu, H.J., Zhang, W. & Chen, X.F., 2009. Two-dimensional seismic wave simulation in anisotropic media by non-staggered finite difference method, *Chin. J. Geophys.,* **52**(6), 1536–1546.

APPENDIX A: SECOND-ORDER STIFFNESS TENSOR FOR ISOTROPIC, VTI AND GENERAL ANISOTROPIC MEDIA

The stress–strain relation for a general anisotropic medium (eq. 2) can be written in a vector–matrix form adopting the Voigt notation,

$$\begin{pmatrix}\sigma_{\theta\theta}\\ \sigma_{\phi\phi}\\ \sigma_{rr}\\ \sigma_{\phi r}\\ \sigma_{\theta r}\\ \sigma_{\theta\phi}\end{pmatrix}=\begin{pmatrix}C_{11}&C_{12}&C_{13}&C_{14}&C_{15}&C_{16}\\ C_{21}&C_{22}&C_{23}&C_{24}&C_{25}&C_{26}\\ C_{31}&C_{32}&C_{33}&C_{34}&C_{35}&C_{36}\\ C_{41}&C_{42}&C_{43}&C_{44}&C_{45}&C_{46}\\ C_{51}&C_{52}&C_{53}&C_{54}&C_{55}&C_{56}\\ C_{61}&C_{62}&C_{63}&C_{64}&C_{65}&C_{66}\end{pmatrix}\begin{pmatrix}\varepsilon_{\theta\theta}\\ \varepsilon_{\phi\phi}\\ \varepsilon_{rr}\\ 2\varepsilon_{\phi r}\\ 2\varepsilon_{\theta r}\\ 2\varepsilon_{\theta\phi}\end{pmatrix}. \qquad \text{(A1)}$$

In the regions where the structure doesn't exhibit anisotropy and the medium is isotropic, the stiffness tensor is composed of only two independent Lamé parameters λ and μ,

$$\mathbf{C}=\begin{pmatrix}\lambda+2\mu&\lambda&\lambda&0&0&0\\ \lambda&\lambda+2\mu&\lambda&0&0&0\\ \lambda&\lambda&\lambda+2\mu&0&0&0\\ 0&0&0&\mu&0&0\\ 0&0&0&0&\mu&0\\ 0&0&0&0&0&\mu\end{pmatrix}. \qquad \text{(A2)}$$

Because the Earth exhibits anisotropy symmetric with respect to the r-axis in large scale, a hexagonal anisotropy with the symmetry axis coincident with r-axis, the so-called vertical transversely isotropic (VTI) or radial anisotropy, is commonly used in seismology. The stiffness tensor of a VTI medium has five independent parameters (Love 1927),

$$\mathbf{C}=\begin{pmatrix}A&A-2N&F&0&0&0\\ A-2N&A&F&0&0&0\\ F&F&C&0&0&0\\ 0&0&0&L&0&0\\ 0&0&0&0&L&0\\ 0&0&0&0&0&N\end{pmatrix}. \qquad \text{(A3)}$$

These parameters are related to the anisotropic parameters of the PREM (Dziewonski & Anderson 1981) through $A=\rho V_{PH}^2$, $C=\rho V_{PV}^2$, $N=\rho V_{SH}^2$, $L=\rho V_{SV}^2$ and $F/(A-2L)=\eta$. F is a function of velocities at intermediate incidence angles. The collocated-grid finite-difference scheme adopted in this study (shown in the next section) can easily handle the VTI or general anisotropic media.

APPENDIX B: COEFFICIENT MATRICES OF THE COMPACT VECTOR–MATRIX EQUATION

Expressions of the coefficient matrices $\mathbf{A}_\theta$, $\mathbf{A}_\phi$, $\mathbf{A}_r$ and $\mathbf{A}$ introduced in eq. (22) are

$$\mathbf{A}_\theta=\frac{1}{r}\begin{bmatrix}0&0&0&\frac{1}{\rho}&0&0&0&0&0\\ 0&0&0&0&0&0&0&0&\frac{1}{\rho}\\ 0&0&0&0&0&0&0&\frac{1}{\rho}&0\\ C_{11}&C_{16}&C_{15}&0&0&0&0&0&0\\ C_{12}&C_{26}&C_{25}&0&0&0&0&0&0\\ C_{13}&C_{36}&C_{35}&0&0&0&0&0&0\\ C_{14}&C_{46}&C_{45}&0&0&0&0&0&0\\ C_{15}&C_{56}&C_{55}&0&0&0&0&0&0\\ C_{16}&C_{66}&C_{56}&0&0&0&0&0&0\end{bmatrix}, \qquad \text{(B1)}$$

$$\mathbf{A}_\phi = \frac{1}{r\sin\theta}\begin{bmatrix} 0 & 0 & 0 & 0 & 0 & 0 & 0 & 0 & \frac{1}{\rho} \\ 0 & 0 & 0 & 0 & \frac{1}{\rho} & 0 & 0 & 0 & 0 \\ 0 & 0 & 0 & 0 & 0 & 0 & \frac{1}{\rho} & 0 & 0 \\ C_{16} & C_{12} & C_{14} & 0 & 0 & 0 & 0 & 0 & 0 \\ C_{26} & C_{22} & C_{24} & 0 & 0 & 0 & 0 & 0 & 0 \\ C_{36} & C_{23} & C_{34} & 0 & 0 & 0 & 0 & 0 & 0 \\ C_{46} & C_{24} & C_{44} & 0 & 0 & 0 & 0 & 0 & 0 \\ C_{56} & C_{25} & C_{45} & 0 & 0 & 0 & 0 & 0 & 0 \\ C_{66} & C_{26} & C_{46} & 0 & 0 & 0 & 0 & 0 & 0 \end{bmatrix}, \tag{B2}$$

$$\mathbf{A}_r = \begin{bmatrix} 0 & 0 & 0 & 0 & 0 & 0 & 0 & \frac{1}{\rho} & 0 \\ 0 & 0 & 0 & 0 & 0 & 0 & \frac{1}{\rho} & 0 & 0 \\ 0 & 0 & 0 & 0 & 0 & \frac{1}{\rho} & 0 & 0 & 0 \\ C_{15} & C_{14} & C_{13} & 0 & 0 & 0 & 0 & 0 & 0 \\ C_{25} & C_{24} & C_{23} & 0 & 0 & 0 & 0 & 0 & 0 \\ C_{35} & C_{34} & C_{23} & 0 & 0 & 0 & 0 & 0 & 0 \\ C_{45} & C_{44} & C_{34} & 0 & 0 & 0 & 0 & 0 & 0 \\ C_{55} & C_{45} & C_{35} & 0 & 0 & 0 & 0 & 0 & 0 \\ C_{56} & C_{46} & C_{36} & 0 & 0 & 0 & 0 & 0 & 0 \end{bmatrix}, \tag{B3}$$

$$\mathbf{A} = \frac{1}{r}\begin{bmatrix} 0 & 0 & 0 & \frac{\cot\theta}{\rho} & -\frac{\cot\theta}{\rho} & 0 & 0 & \frac{3}{\rho} & 0 \\ 0 & 0 & 0 & 0 & 0 & 0 & \frac{3}{\rho} & 0 & \frac{2\cot\theta}{\rho} \\ 0 & 0 & 0 & -\frac{1}{\rho} & -\frac{1}{\rho} & \frac{2}{\rho} & 0 & \frac{\cot\theta}{\rho} & 0 \\ \cot\theta\, C_{12} - C_{15} & -C_{14} - \cot\theta\, C_{16} & C_{11} + C_{12} & 0 & 0 & 0 & 0 & 0 & 0 \\ \cot\theta\, C_{22} - C_{25} & -C_{24} - \cot\theta\, C_{26} & C_{12} + C_{22} & 0 & 0 & 0 & 0 & 0 & 0 \\ \cot\theta\, C_{23} - C_{35} & -C_{34} - \cot\theta\, C_{36} & C_{13} + C_{23} & 0 & 0 & 0 & 0 & 0 & 0 \\ \cot\theta\, C_{24} - C_{45} & -C_{44} - \cot\theta\, C_{36} & C_{14} + C_{24} & 0 & 0 & 0 & 0 & 0 & 0 \\ \cot\theta\, C_{25} - C_{55} & -C_{45} - \cot\theta\, C_{56} & C_{15} + C_{25} & 0 & 0 & 0 & 0 & 0 & 0 \\ \cot\theta\, C_{26} - C_{56} & -C_{46} - \cot\theta\, C_{66} & C_{16} + C_{26} & 0 & 0 & 0 & 0 & 0 & 0 \end{bmatrix}. \tag{B4}$$